Inverse design of three-dimensional multicellular biobots with target functions

Hui-Kai Zhang, Bo-Wen Xu, Zi-Yao Jia, Bo Li, Xi-Qiao Feng [*]

Department of Engineering Mechanics, AML, Institute of Biomechanics and Medical Engineering, Tsinghua University, Beijing 100084, China

ABSTRACT

Hybrid living biobots consisting of active cells hold promise for significant applications as, for example, intelligent devices in medical engineering and organisms with specific functions in synthetic biology. However, the design and creation of living biobots with various cells remain a challenge. In this paper, we propose a three-dimensional inverse optimization strategy based on the pixel topology optimization method, to design self-propelled living biobots with the function of biomechanical actuations. For illustration, we design several biobots composed of active and passive elements that mimic cardiomyocytes and passive epidermal cells sourced from such as *Xenopus laevis*, human induced pluripotent stem cells or neonatal rats. Their topologies are optimized by implementing the active constitutive relations of cells into the multicellular topological interpolation model. Effects of nutrient concentrations, elasticity, and anisotropic contraction of cardiomyocytes on the topologies and functionalities of the biobots are examined. In addition, we unveil the living topological interfaces generated by the collective actuations of the optimized biobots. We show a potential of collective biobots for high-throughput drug screening owing to their distinct biomechanical responses under healthy and sick conditions. The proposed inverse optimization method can be extended to design various functional multicellular biological systems, which impacts the studies of organ development, synthetic biology, and medical engineering.

1. Introduction

Robots, such as Atlas and SpotMini, offer a wide range of applications in both industries [Fig. 1(a and b)] and our daily lives. In our bodies, there are billions of small biobots, including DNA motor proteins (Bath et al., 2009), ATP synthases (Elston et al., 1998), myosin (Mizuno et al., 2007; Regazzoni et al., 2021), and dynein motor proteins (Jia et al., 2022; Nitta et al., 2021), each performing vital biological functions. For instance, DNA motors function like factories, continuously carrying out DNA transcription, replication, and repair processes. The rotational ability of molecular complexes F0 and F1 in ATP synthase (Noj et al., 1997) provides the cells with the required energy to sustain their biological functions. Additionally, by adjusting the conformation of the heads in myosin-II, thick myofilaments can slide along thin myofilaments, yielding proper activity of cardiomyocytes (Avazmohammadi et al., 2019; Regazzoni et al., 2021). Unlike microscale intelligent robots that utilize piezoelectric materials [Fig. 1(c)] (Cui et al., 2022) or flexible electronic devices (Cheng et al., 2023), biobots are composed of active cells [Fig. 1(d–f)], living motor proteins [Fig. 1(g–j)], and other components. They are created to achieve specific biological and medical functions.

---

* Corresponding author.
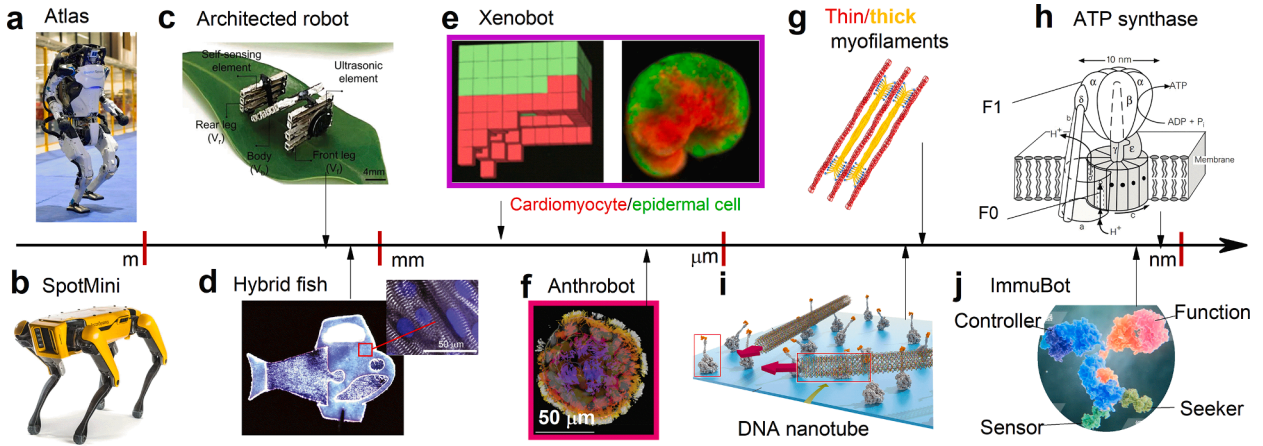 *E-mail address:* fengxq@tsinghua.edu.cn (X.-Q. Feng).

Fig. 1. Robots at different scales. (a,b) Atlas and SpotMini (https://www.bostondynamics.com/). (c) Active architected robot. Adopted from Cui et al. (2022) with permission. (d) Hybrid biological fish. Adopted from Lee et al. (2022) with permission. (e) *Xenobot* composed of cardiomyocytes (red voxels) and epidermal cells (green voxels). Adopted from Kriegmana et al. (2020) with permission. (f) Motile living anthrobot self-construct from adult human somatic progenitor seed cells *in vitro*. Adopted from Gumuskaya et al. (2023) with permission. (g) Thin myofilaments (red) and thick actin filaments (yellow). (h) ATP synthases. Adopted from Elston et al. (1998) with permission. (i) Living material driven by dynein proteins. Adopted from Ibusuki et al. (2022) with permission. (j) ImmuBot composed of diverse protein molecules (https://www.biomap. com/zh/research-projects/).
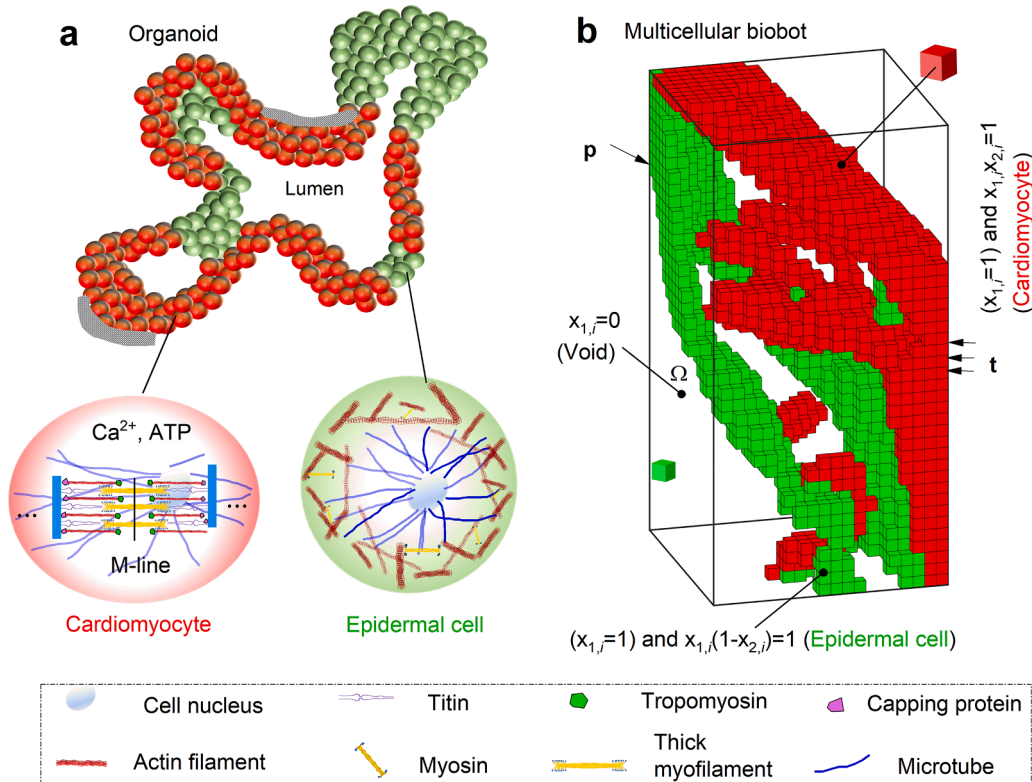

Fig. 2. Topological model of an organoid consisting of two types of cells. (a) An organoid composed of cardiomyocytes (red) and epidermal cells (green). (b) An optimized multicellular biobot. In the design domain, the void and solid regions are marked by $x_1 = 0$ and $x_1 = 1$, respectively. The solid regions are filled with either cardiomyocytes denoted by $x_1 x_2 = 1$ or epidermal cells denoted by $x_1 (1 - x_2) = 1$. Ω is the design domain.

Recently, the design of hybrid biobots, combining living cells with artificial materials, has gained much attention (Feinberg et al., 2007; Gao et al., 2021; Guix et al., 2021; Jia et al., 2022; Lee et al., 2022; Nitta et al., 2021; Wang et al., 2022). In a pioneering work, Feinberg et al. (2007) combined cardiomyocytes and artificial Polydimethylsiloxane thin films to create active structures that can

swim, opening up new opportunities to design hybrid biobots (Guix et al., 2021). This methodology has been employed to create cellular fishes (Lee et al., 2022; Park et al., 2016) and cell-based medical devices (Alford et al., 2010; Lee et al., 2022; Lind et al., 2017). Moreover, biological myosin-II or dynein proteins have been utilized to design hybrid living biobots for structural actuation (Jia et al., 2022; Nitta et al., 2021) or cargo delivery (Ibusuki et al., 2022). Advances in cell assembly (Gumuskaya et al., 2023) and printing technologies enable us to produce three-dimensional (3D) cell spheroids (Ao et al., 2022; Stevens et al., 2023; Toda et al., 2018), organoids (LeSavage et al., 2022; Ren and Han, 2019; Takebe and Wells, 2019; Tuveson and Clevers, 2019), and printed tissues (Luo et al., 2022; Ravanbakhsh and Zhang, 2022; Xue et al., 2023) consisting of various types of cells. This has paved a novel route to making living biobots with approximately designed topologies and functionalities.

Through a combination of numerical simulations and experiments, Kriegmana et al. (2020) designed a *Xenobot* made up of *Xenopus laevis* cardiomyocytes and epidermal cells. They constructed an active isotropic spring model to describe the periodic contraction of cardiomyocytes. Using a multicellular assembly technology, they optimized the organ with the locomotion ability being the objective function (Kriegman et al., 2021, 2020). Moreover, Gumuskaya et al. (2023) synthesized multicellular motile biobots starting from one adult human lung cell, named Anthrobot. This type of biobot can promote gap closures on scratched live neuronal monolayer tissues in vitro. These organisms have simple 3D topologies without complex holes and structs (Kriegmana et al., 2020), which rely on the functional requirements. Recently, the rapidly developing cryo-bioprinting (Luo et al., 2022; Ravanbakhsh and Zhang, 2022) and multi-axis robot-based bioprinting techniques (Zhang et al., 2022b) make it possible to produce complex topologies of 3D organisms composed of various types of cells. These multicellular topological structures not only endow the organs with specific biological functions and but also impact the morphogenesis in the processes of embryo development. Moreover, the biomechanical behaviors of cells, such as elastic deformation and active contraction, play a crucial role in the topologies and functions of organisms. However, there is a lack of a theoretical method that incorporates these complex cellular behaviors and topologies into the design of biobots.

In this paper, we establish a 3D pixel multicellular inverse optimization method based on the solid-isotropic-material-with-penalization (SIMP) interpolation model (Aage et al., 2017; Zhang et al., 2022a). In this case, each element mesh in the design domain represents an active cardiomyocyte, a passive epidermal cell, or a void (Bendsoe and Sigmund, 1999). For illustration, we will optimize the specific actuation of biobots consisting of two types of cells. The model also includes the effects of anisotropic contractions and nutrient concentrations. Moreover, we will unveil novel collective biobot behaviors, which offer great potential for designing biological intelligent systems, such as drug screening (Ao et al., 2022; Goldfracht et al., 2019; Mills et al., 2019) or living topological materials (Jiang et al., 2022).

2. Active mechanics model of cardiomyocytes

Fig. 2(a) schematically shows an organoid composed of cardiomyocytes (red) and epidermal cells (green). The cardiomyocytes exhibit active contraction ability, resulting from the relative movements of thick and thin filaments driven by ATP and Ca^{2+} ions (Avazmohammadi et al., 2019; Regazzoni et al., 2021). They have higher stiffness than the epidermal cells. The effective active stress field model, combined with the finite element method (FEM), has been proposed to simulate such biomechanical problems (Bol et al., 2009; Goktepe et al., 2010; Goriely, 2018; Kaczmarski et al., 2023; Paetsch et al., 2012; Sato et al., 2021; Yuhn et al., 2023).

As shown in Fig. 2(b), the biobot is composed of 3D cubic voxels, each having an average size of about $100 \times 100 \times 100$ μm^3 (Kriegmana et al., 2020). The red voxels represent the cardiomyocytes with active contraction ability; while the green voxels represent the passive epidermal cells. Although the two types of cells have a significant difference in morphology, our model can not only efficiently capture their biomechanical behaviors of current interest by introducing their active constitutive relations, but also describe the topological layouts. In the context of optimized biobots, the cubic voxels in the figures refer to the cells, while in the calculation models of the design domains, they represent the finite element meshes.

To represent the active stresses generated by the cardiomyocytes (red voxels), their active constitutive relation is expressed as

$$\boldsymbol{\sigma}_{\mathrm{ela}} = \mathbf{D}(\boldsymbol{\varepsilon} - \boldsymbol{\varepsilon}_{\mathrm{a}}) = \boldsymbol{\sigma} - \boldsymbol{\sigma}_{\mathrm{a}}, \tag{1}$$

where $\boldsymbol{\sigma} = \mathbf{D}\boldsymbol{\varepsilon}$ is the total stress, $\boldsymbol{\sigma}_{\mathrm{ela}}$ and $\boldsymbol{\sigma}_{\mathrm{a}} = \mathbf{D}\boldsymbol{\varepsilon}_{\mathrm{a}}$ denote the elastic and active stresses, respectively; $\mathbf{D}(v, E_c)$ is the elastic matrix with v and E_c being the Poisson's ratio and elastic modulus of the cardiomyocytes, respectively; $\boldsymbol{\varepsilon}$ and $\boldsymbol{\varepsilon}_{\mathrm{a}}$ are the total and the active strain, respectively. The active strain is written as

$$\boldsymbol{\varepsilon}_{\mathrm{a}} = \Delta C \left[\alpha_x, \alpha_y, \alpha_z, 0, 0, 0 \right]^{\mathrm{T}}, \tag{2}$$

where ΔC is the nutrient concentration (e.g., ATP or Ca^{2+} ions) (Avazmohammadi et al., 2019; Regazzoni et al., 2021). α_x, α_y, and α_z are the contraction coefficients of the red voxels in the x, y, and z-directions, respectively. In Eq. (2), if the nutrient concentration ΔC is set to zero, the active strain $\boldsymbol{\varepsilon}_{\mathrm{a}}$ will disappear. Consequently, the stress of passive epidermal cells in Eq. (1) will degenerate to $\boldsymbol{\sigma}_{\mathrm{ela}} = \mathbf{D}(v, E_e)\boldsymbol{\varepsilon} = \boldsymbol{\sigma}$, where E_e is the elastic modulus of epidermal cells.

The total potential energy function of the organism in Fig. 2(b) can be written as

$$\Pi(\mathbf{u}_i) = \sum_{i=1}^{N} \int_{\Omega_i} \left[\frac{1}{2} \boldsymbol{\varepsilon}^{\mathrm{T}} \mathbf{D}(v, E_i) \boldsymbol{\varepsilon} - \boldsymbol{\varepsilon}^{\mathrm{T}} \mathbf{D}(v, E_i) \boldsymbol{\varepsilon}_{\mathrm{a}} \left(\widetilde{\alpha}_{i,x}, \widetilde{\alpha}_{i,y}, \widetilde{\alpha}_{i,z} \right) - \mathbf{u}_i^{\mathrm{T}} \mathbf{p} \right] d\Omega_i$$

$$- \sum_{i=1}^{N} \int_{\Gamma_\sigma^i} \mathbf{u}_i^{\mathrm{T}} \mathbf{t} \, d\Gamma^i, \tag{3}$$

where $\mathbf{u}_i$ denotes the displacement vector of the ith element mesh, N is the total number of the element meshes in the design domain Ω, Ω_i and Γ_σ^i are the space and surface force boundaries of the ith element mesh, $\mathbf{p}$ and $\mathbf{t}$ represent the external nodal and surface forces, respectively. E_i ($i = 1, 2, ..., N$) and $\widetilde{\alpha}_{i,m}$ ($m = x, y, z$) are the Young's modulus and contraction coefficients of the ith element mesh, respectively. In the following Section 3.1, we will establish a topological model to determine the values of $E_i = E_c$, E_e, or 0 and $\widetilde{\alpha}_{i,m} = \alpha_m$ or 0 in the ith element mesh.

By using Eq. (1), and employing the variational principle, we can obtain the governing equation

$$\mathbf{K}\mathbf{u} = \mathbf{P} + \mathbf{P}_t + \mathbf{P}_{bio-chemo}, \tag{4}$$

where $\mathbf{K}$ and $\mathbf{u}$ denote the global stiffness matrix and displacement vector, respectively. The nodal and surface forces are expressed as

$$\mathbf{P} = \sum\nolimits_{i=1}^{N} \int_{\Omega_i} \mathbf{N}^T \mathbf{p} \, d\Omega_i, \tag{5}$$

$$\mathbf{P}_t = \sum\nolimits_{i=1}^{N} \int_{\Gamma_\sigma^i} \mathbf{N}^T \mathbf{t} \, d\Gamma^i, \tag{6}$$

where $\mathbf{N}$ is the matrix of shape function in the FEM, and the active force is

$$
\begin{aligned}
\mathbf{P}_{bio-chemo} &= \sum_{i=1}^{N} \int_{\Omega_i} \mathbf{B} \mathbf{D}(E_i) \boldsymbol{\varepsilon}_a(\widetilde{\alpha}_{i,m}) d\Omega_i \\
&= \sum_{i=1}^{N} \sum_{i_g=1}^{n_g} \widetilde{\mathbf{B}}\left(\xi_{i_g}, \eta_{i_g}, \zeta_{i_g}\right) \mathbf{D}(E_i) \boldsymbol{\varepsilon}_a(\widetilde{\alpha}_{i,m}) |\mathbf{J}| H_{ig}.
\end{aligned}
\tag{7}
$$

These forces provide a framework for analyzing the biomechanical behaviors of the organism. For simplicity, we disregard the forces $\mathbf{P}$ and $\mathbf{P}_t$, and primarily focus on the effects of active biological force $\mathbf{P}_{bio-chemo}$.

3. Multicellular topology optimization method

In this section, we propose a topology optimization framework to optimize the cardiomyocyte and epidermal cell distributions in a multicellular organism or biological robot [Fig. 2(b)] that possesses specific biomechanical functions, for example, actuation. We first introduce a multicellular interpolation model and a filtering method based on the discretized design parameters. Subsequently, we propose the optimization formulation and show the details of the calculation process of sensitivity information.

3.1. Interpolation model and filtering technique

Based on the SIMP model (Aage et al., 2017; Gao and Zhang, 2010; Sigmund, 2001b), E_i and $\widetilde{\alpha}_{i,m}$ are written as

$$E_i(x_{1,i}, x_{2,i}) = x_{1,i}^{\eta_1}\left[x_{2,i}^{\eta_2} E_c + \left(1 - x_{2,i}^{\eta_2}\right)E_e\right], i = 1, 2, ..., N, \tag{8}$$

$$\widetilde{\alpha}_{i,m}(x_{1,i}, x_{2,i}) = x_{1,i}^{\eta_1} x_{2,i}^{\eta_2} \alpha_m, m = x, y, z, \tag{9}$$

where $x_{1,i}$ and $x_{2,i} \in [0, 1]$ are the two types of design variables that can tune the distributions of cells in the design domain Ω [Fig. 2(b)]. The penalty factors $\eta_1 = \eta_2 = 4.0$ are introduced to facilitate the values of $x_{1,i}$, $x_{2,i}$ to 0 or 1.

To avoid the occurrence of checkboard patterns in the SIMP method (Aage et al., 2017; Bendsoe and Sigmund, 1999; Sigmund and Torquato, 1997), we take the following filtering operators

$$\rho_{1,i} = \frac{\sum_{j \in N_i} w(\mathbf{r}_i, \mathbf{r}_j) v_j x_{1,j}}{\sum_{j \in N_i} w(\mathbf{r}_i, \mathbf{r}_j) v_j}, \tag{10}$$

$$\rho_{2,i} = \frac{\sum_{j \in N_i} w(\mathbf{r}_i, \mathbf{r}_j) v_j x_{2,j}}{\sum_{j \in N_i} w(\mathbf{r}_i, \mathbf{r}_j) v_j}, \tag{11}$$

where $N_i = \{j = \| \mathbf{r}_i - \mathbf{r}_j \| \le R\}$, $R = 150 \, \mu m$ is the filtering radius. $\mathbf{r}_i$ and $\mathbf{r}_j$ are the position vectors of element meshes i and j ($j \in N_i$), respectively. $w(\mathbf{r}_i, \mathbf{r}_j) = \max(0, R - \| \mathbf{r}_i - \mathbf{r}_j \|)$ is the weight factor, and v_j is the volume of the element. Moreover, the increase of R can enhance the robustness of the optimized structures. As a result of filtering, the physical densities are also restricted to the interval [0, 1]. Then the elastic modulus and contraction coefficients of the ith element mesh are rewritten as

$$E_i = \rho_{1,i}^{\eta_1}\left[\rho_{2,i}^{\eta_2} E_c + \left(1 - \rho_{2,i}^{\eta_2}\right)E_e\right], \tag{12}$$

$$\widetilde{\alpha}_{i,m} = \rho_{1,i}^{\eta_1} \rho_{2,i}^{\eta_2} \alpha_m. \tag{13}$$

Finally, the values of E_i [Fig. 2(b)] and $\widetilde{\alpha}_{i,m}$ of the ith element mesh are

$$
\begin{cases}
E_i \to 0, \ \widetilde{\alpha}_{i,m} \to 0, \ \text{(Voids)} & \text{if } x_{1,\ i} \to 0, \\
E_i \to E_c, \ \widetilde{\alpha}_{i,m} \to \alpha_m, \ \text{(Cardiomyocytes)} & \text{if } x_{1,\ i} \to 1 \text{ and } x_{2,\ i} \to 1, \\
E_i \to E_e, \ \widetilde{\alpha}_{i,m} \to 0, \ \text{(Epidermal cells)} & \text{if } x_{1,\ i} \to 1 \text{ and } x_{2,\ i} \to 0.
\end{cases}
\tag{14}
$$

3.2. Biomechanical function analysis

To achieve the desired function of the biobot, one may require that the target nodal displacements at a specific position satisfy a prescribed condition. This strategy has been employed in the design of microdevices that can quickly respond to external stimuli (Chen. et al., 2023; Geiss et al., 2019; Hamel et al., 2019; Tian et al., 2022; Zhao and Zhang, 2022), such as forces (Sigmund, 2001a), electrical fields (Sigmund, 2001b), or fluid pressures (Kumar and Langelaar, 2021). In this case, the function is formulated as

$$
\text{min or max} : J = u_q = \mathbf{L}_q^{\mathrm{T}} \mathbf{u},
\tag{15}
$$

where u_q is the output displacement of the qth target point, and $\mathbf{L}_q$ is the corresponding unit index vector. The choice of 'min' or 'max' depends on the requirements. In the case, the maximum output work done by the optimized organism is written as

$$
\text{max} : \ W = 1 \big/ 2 k_q |u_q|^2,
\tag{16}
$$

where k_q represents the effective stiffness of the system along the output direction. Here we take the value of $k_q = 10^{-8}$ N /μm.

3.3. Optimization of multicellular biobots

To obtain the unknown topology in the multicellular biobot with minimizing nodal displacements, such as the nodal movements along the negative y-direction, the optimization method reads

$$
\begin{aligned}
&\text{find} : \ \mathbf{x}_1 = \left(x_{1,\ 1}, \ x_{1,\ 2}, ..., \ x_{1,\ N}\right)^{\mathrm{T}}, \ \mathbf{x}_2 = \left(x_{2,\ 1}, \ x_{2,\ 2}, ..., \ x_{2,\ N}\right)^{\mathrm{T}} \\
&\min_{\mathbf{x}_1, \mathbf{x}_2} : \ J = \sum_q \mathbf{L}_q^{\mathrm{T}} \mathbf{u} \\
&\text{s.t.} :
\begin{cases}
\mathbf{K}(\mathbf{x}_1, \ \mathbf{x}_2)\mathbf{u} = \mathbf{P}_{\text{bio-chemo}}(\mathbf{x}_1, \mathbf{x}_2), \\
V_c(\mathbf{x}_1, \ \mathbf{x}_2) \leq V_c^*, \\
V_e(\mathbf{x}_1, \ \mathbf{x}_2) \leq V_e^*, \\
0 \leq x_{1,\ i} \leq 1, \ \ 0 \leq x_{2,\ i} \leq 1, \ (i = 1, \ 2, \cdots, \ N),
\end{cases}
\end{aligned}
\tag{17}
$$

where the vectors $\mathbf{x}_1$ and $\mathbf{x}_2$ denote the topological design variables as defined in Eqs. (8) and (9). Furthermore, the volume fractions of cardiomyocytes and epidermal cells are calculated respectively by

$$
V_c(\mathbf{x}_1, \mathbf{x}_2) = \sum_i^N \frac{s_i \rho_{1,\ i} \rho_{2,\ i}}{\Omega},
\tag{18}
$$

$$
V_e(\mathbf{x}_1, \mathbf{x}_2) = \sum_i^N \frac{s_i \rho_{1,\ i}\left(1 - \rho_{2,\ i}\right)}{\Omega},
\tag{19}
$$

where s_i and Ω are the volumes of the ith element mesh and the design domain before optimization starting, respectively.

3.4. Sensitivity analysis

To obtain the optimization results in Eq. (17), the topology design variables $\mathbf{x}_1$ and $\mathbf{x}_2$ should be updated through iterations. Based on the gradient optimization method, such as MMA (Svanberg, 1987), the optimal search directions are determined by the gradient information of the objective function and constraints with respect to the design variables.

In Eq. (17), the objective function depends on the displacement vector $\mathbf{u}$, and its gradient information contains $\partial \mathbf{u} / \partial x_{k,i}$, $(k = 1,2)$. Though it can be obtained by taking the derivates of the functions in Eq. (17), this process is cumbersome. Typically, an adjoint method is effective to avoid explicitly calculating the derivates of displacements $\partial \mathbf{u} / \partial x_{k,i}$, and the objective function in Eq. (17) can be rewritten as

$$
\ell = J + \boldsymbol{\lambda}^{\mathrm{T}}(\mathbf{Ku} - \mathbf{P}_{\text{bio-chemo}}) = \sum_q \mathbf{L}_q^{\mathrm{T}} \mathbf{u} + \boldsymbol{\lambda}^{\mathrm{T}}(\mathbf{Ku} - \mathbf{P}_{\text{bio-chemo}}),
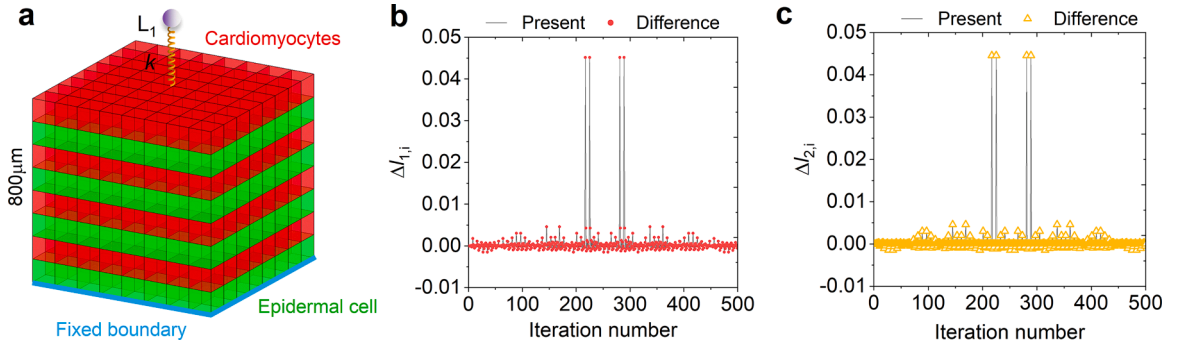\tag{20}
$$

Fig. 3. Validation of sensitivity analysis. (a) A sheet-like multicellular organism is depicted. (b) Sensitivity information of $\rho_{1,\,i}$. (c) Sensitivity information of $\rho_{2,\,i}$.

where λ represents a nonzero arbitrary adjoint vector. The derivates of the new objective function in Eq. (20) can be obtained as

$$
\begin{aligned}
\frac{\partial \ell}{\partial x_{k,\,i}} &= \sum_q \mathbf{L}_q^{\mathrm{T}} \frac{\partial \mathbf{u}}{\partial x_{k,\,i}} + \lambda^{\mathrm{T}} \left(\frac{\partial \mathbf{K}}{\partial x_{k,\,i}} \mathbf{u} + \mathbf{K} \frac{\partial \mathbf{u}}{\partial x_{k,\,i}} - \frac{\partial \mathbf{P}_{\mathrm{bio-chemo}}}{\partial \mathbf{x}_{k,\,i}} \right) \\
&= \left(\lambda^{\mathrm{T}} \frac{\partial \mathbf{K}}{\partial x_{k,\,i}} \mathbf{u} - \lambda^{\mathrm{T}} \frac{\partial \mathbf{P}_{\mathrm{bio-chemo}}}{\partial x_{k,\,i}} \right) + \left(\lambda^{\mathrm{T}} \mathbf{K} \frac{\partial \mathbf{u}}{\partial x_{k,\,i}} + \sum_q \mathbf{L}_q^{\mathrm{T}} \frac{\partial \mathbf{u}}{\partial x_{k,\,i}} \right)
\end{aligned}
\tag{21}
$$

The second term in Eq. (21) can be ignored if the nonzero vector λ satisfies

$$
\lambda^{\mathrm{T}} \mathbf{K} + \sum_q \mathbf{L}_q^{\mathrm{T}} = \mathbf{0},
\tag{22}
$$

In this case, Eq. (21) reduces to

$$
\frac{\partial \ell}{\partial \mathbf{x}_{k,\,i}} = \lambda^{\mathrm{T}} \frac{\partial \mathbf{K}}{\partial x_{k,\,i}} \mathbf{u} - \lambda^{\mathrm{T}} \frac{\partial \mathbf{P}_{\mathrm{bio-chemo}}}{\partial \mathbf{x}_{k,\,i}},
\tag{23}
$$

Substituting Eqs. (12) and (13) into Eq. (23) leads to

$$
\frac{\partial \ell}{\partial x_{k,\,i}} = \lambda_i^{\mathrm{T}} \frac{\partial E_i(\mathbf{x}_1, \mathbf{x}_2)}{\partial x_{k,\,i}} \mathbf{k}_i \mathbf{u}_i - \lambda^{\mathrm{T}} \frac{\partial \left[E_i(\mathbf{x}_1, \mathbf{x}_2) \widetilde{\alpha}_{i,m}(\mathbf{x}_1, \mathbf{x}_2) \right]}{\partial x_{k,\,i}} \widetilde{\mathbf{P}}_{i,\,\mathrm{bio-chemo}},
\tag{24}
$$

where the terms $\partial E_i / \partial x_{k,i}$ and $\partial (E_i \widetilde{\alpha}_{i,m})/\partial x_{k,i}$ can be calculated from Eqs. (12) and (13).

Furthermore, the derivates of the volume fractions of cardiomyocytes and epidermal cells with respect to the design variables are

$$
\frac{\partial V_{\mathrm{c}}(\mathbf{x}_1, \mathbf{x}_2)}{\partial x_{k,i}} = \frac{\partial}{\partial x_{k,\,i}} \sum_i \frac{\rho_{1,\,i} \rho_{2,\,i} s_i}{\Omega} = \frac{\partial \left(\rho_{1,\,i} \rho_{2,\,i} \right)}{\partial x_{k,\,i}} \frac{s_i}{\Omega},
\tag{25}
$$

$$
\frac{\partial V_{\mathrm{e}}(\mathbf{x}_1, \mathbf{x}_2)}{\partial x_{k,\,i}} = \frac{\partial}{\partial x_{k,\,i}} \sum_i \frac{\rho_{1,\,i} (1 - \rho_{2,\,i}) s_i}{\Omega} = \frac{\partial \left[\rho_{1,\,i} (1 - \rho_{2,\,i}) \right]}{\partial x_{k,\,i}} \frac{s_i}{\Omega},
\tag{26}
$$

where the terms $\partial(\rho_{1,\,i} \rho_{2,\,i})/\partial x_{k,\,i}$ and $\partial \left[\rho_{1,\,i} (1 - \rho_{2,\,i}) \right]/\partial x_{k,\,i}$ can be calculated from Eqs. (10) and (11).

We use the difference method to verify the derivatives of the objective functions, as shown in Fig. 3(a), where the depicted biobot consists of $n_x \times n_y \times n_z = 8 \times 8 \times 8$ cells. The volume fractions of cardiomyocytes and epidermal cells are set as $V_{\mathrm{c}}^* = V_{\mathrm{e}}^* = 50\%$. The nutrient concentration and active contraction coefficients are specified as $\Delta C = 0.5$ and $\alpha_x = \alpha_y = \alpha_z = -0.1$, respectively. The elastic moduli of cardiomyocytes and epidermal cells are set as $E_{\mathrm{c}} = 100$ kPa and $E_{\mathrm{e}} = 10$ kPa, respectively; and their Poisson's ratio is assumed to be $\nu = 0.3$ (Mathur et al., 2001).

The sensitivities calculated by the difference method are expressed as

$$
\Delta \ell_{1,\,i} = \frac{\ell(\rho_{1,\,i} + \Delta a, \boldsymbol{\rho}_2) - \ell(\boldsymbol{\rho}_1, \boldsymbol{\rho}_2)}{\Delta a},
\tag{27}
$$

$$
\Delta \ell_{2,\,i} = \frac{\ell(\boldsymbol{\rho}_1, \rho_{2,i} + \Delta a) - \ell(\boldsymbol{\rho}_1, \boldsymbol{\rho}_2)}{\Delta a},
\tag{28}
$$

where $\Delta a = 10^{-3}$ is the perturbation parameter. Notably, in Fig. 3(b and c), the theoretical sensitivity information aligns precisely with the values calculated by the difference method. However, the computational burden associated with the difference method used in

Table 1
Optimization process.

Algorithm: Objective function, constraints, design variables, optimization operator
Initialization :
$n_x,\ n_y,\ n_z,\ \Delta C,\ \alpha_x,\ \alpha_y,\ \alpha_z,\ L_q$ ▷ Geometric information
$R,\ V_c^*,\ V_e^*,\ \mathbf{x}_1^{(0)},\mathbf{x}_2^{(0)},N_{it},w(r_i,\ r_j)$ ▷ All optimization parameters
$\mathbf{x}_1^{(0)} = \{x_{1,i} = 0.8,\ i = 1,2,...,N\},$
$\mathbf{x}_2^{(0)} = \{x_{2,i} = 0.8,\ i = 1,2,...,N\},$ ▷ Initial values of design variables
$m,\ a_0,\ (a_i,\ d_i,\ c_i,\ i = 1,2),\ \mathbf{L}_l,\ \mathbf{U}_u$ ▷ Parameters of MMA
while $\max(|\mathbf{x}_1 - \mathbf{x}_1^*|,\ |\mathbf{x}_2 - \mathbf{x}_2^*|) \leq \delta$ or $N_{it} \geq N_{it}^*$
$\mathbf{K}(\mathbf{x}_1,\mathbf{x}_2)\mathbf{u} = \mathbf{P}_{\text{bio}-\text{chemo}}(\mathbf{x}_1,\mathbf{x}_2){\to}\mathbf{u},\ J$ ▷ Calculate finite element
$V_c(\mathbf{x}_1,\mathbf{x}_2),\ V_e(\mathbf{x}_1,\mathbf{x}_2)$
$\partial J/\partial x_{1,i},\ \partial J/\partial x_{2,i},\ \partial V_c/\partial x_{1,i},\ \partial V_e/\partial x_{2,i}$ ▷ Calculate sensitivity information
start the optimization operator MMA   ▷ Inner optimization starts
$\mathbf{x}_1^n,\ \mathbf{x}_2^n$ ▷ Update design variables at nth step
end
Output results : Iteration history, multicellular topology

sensitivity analysis is enormous. Therefore, the sensitivity information for the objective and constraints is expressed by Eqs. (24)–(26). The entire optimization process is listed in Table 1. All numerical simulations are performed by using Matlab on a workstation with Intel (R) Xeon (R) CPU E5-2699 v4 @ 2.20GHz and 256 RAM.

4. Examples

In this section, we give a few examples to design multicellular biobots with specific functionalities, such as cell-driven actuators and grippers, and collective behaviors.

4.1. Design of a tyrannosaurus-like biobot

In the first example, we validate the proposed method by optimizing a biobot that can achieve the maximum biomechanical actuation along the *y*-direction at a specific node. It is motivated by the vertebrates that have functional organs of heads, spines, and limbs. For instance, their heads, driven by skeleton muscle tissues, can move in different directions (Keller, 2002).

Therefore, we define a design domain with the size of $l_x \times l_y \times l_z = 2 \times 4 \times 2$ mm^3 as shown in Fig. 4(a), which is divided into $n_x \times n_y \times n_z$=20 × 40 × 20 element meshes. The optimization objective function is defined by max : $\mathbf{L}_{q\_y}\mathbf{u}$, $q = 1$ [Fig. 4(a)]. The volume fractions of cardiomyocytes and epidermal cells are set as $V_c^* = V_e^* = 10\%$, with the remaining 80% volume being empty. To avoid the locally optimal problem, the initial values of the design variables in the model are set as $x_{1,i} = x_{2,i} = 0.8$, with $i = 1,2,...,N$. The nutrient concentration and contraction coefficients are set as $\Delta C = 1.0$ and $\alpha_x = \alpha_y = \alpha_z = -0.1$, respectively.

After 100 iterations with 453.64 s of computation time, the objective function and the volume fractions converge to stable values as shown in Fig. 4(b), demonstrating the effectiveness and stability of the proposed method. In the final optimized results, we take the values of $\rho_{1,i}\rho_{2,i} \geq 0.5$ or $\rho_{1,i}(1-\rho_{2,i}) \geq 0.5$ as cardiomyocytes or epidermal cells, respectively, because the voxel densities on the organ boundaries do not strictly reach 0 or 1 in the SIMP model. Compared with the theoretical cell number 1600, the optimized biobot consists of 1582 cardiomyocytes and 1393 epidermal cells, respectively [Fig. 4(b)].

In Fig. 4(b and c), the cardiomyocytes are predominantly located in the outer space due to their higher modulus and active contraction ability. This cellular topology layout is essential to actuate a larger displacement along the *y*-direction at the target node. The resulted displacement is 1341.75 μm, and the final work is calculated to be 9.0×10^{-3} N·μm. In the optimized biobot, a hinge is formed, connecting the head and leg regions [Fig. 4(b)]. The epidermal cells act as the passive abdominal component supporting the active actuating part made of cardiomyocytes. Moreover, the topological architecture of cardiomyocytes and epidermal cells is similar to the muscle distribution observed in *Tyrannosaurus*, with muscle tissues concentrated along its neck, back, and legs to achieve rapid body responses [Fig. 4(c and d)].

In addition, the proposed method can handle complex initial design domains, such as those shown in Fig. 4(e and f). In Fig. 4(e), the design domain is an octant of spherical shape of 3.0 mm in radius. Fig. 4(f) has a hemispherical shell with the outer and inner radii of 3.0 mm and 2.0 mm, respectively. The objective function and the percentage of cell numbers are all consistent with those in Fig. 4(a).

Though the biobots in Fig. 4(e and f) have similar functionalities to that in Fig. 4(b), exhibiting the maximum output along the *y*-direction at specified points (Video S1, Supplementary materials), the initial design domains significantly influence the optimal topologies of the biobots. Therefore, this method can be used to design biobots with complex design domains to meet specific functional requirements.

To illustrate the effects of the total cell number on the optimized organisms, we scale up the characteristic sizes of the biobot, as shown in Fig. 5. We vary the total cell number $(n_x \times n_y \times n_z) \times V_T^*$ from $(20 \times 40 \times 20) \times 20\%$ to $(80 \times 160 \times 80) \times 20\%$, with the
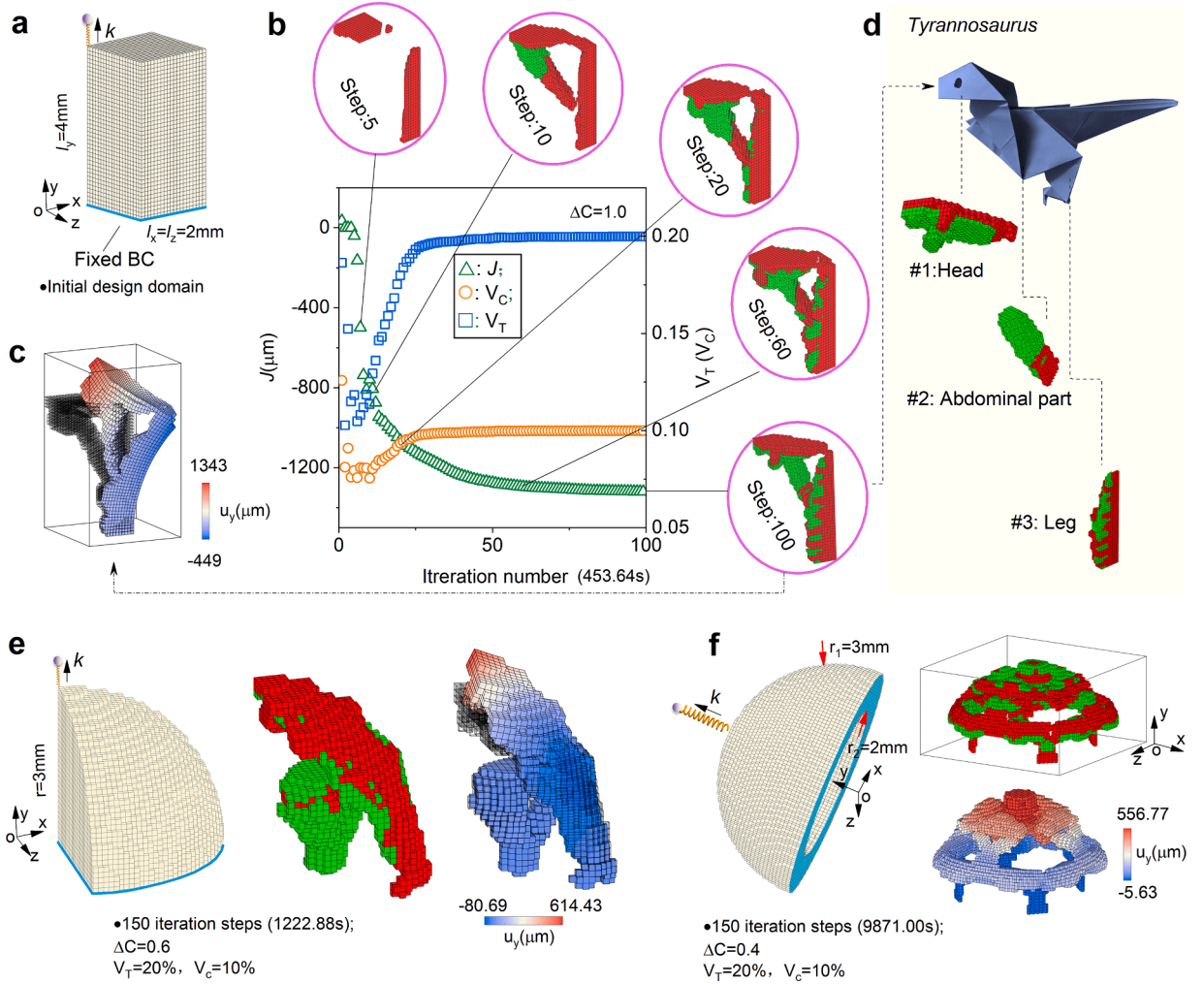
Fig. 4. Validation of the proposed method. (a) A design domain and boundary conditions. (b) Iteration history and computation costs of the objective function and volume fractions. (c) Deformed biobot. (d) Comparison between the optimized multicellular biobot with a *Tyrannosaurus* origami. Optimized biobots in an octant with a spherical shape (e) and a hemispherical shell domain (f). Here, we set the initial values of the design variables as $x_{1,i}^{(0)} = x_{2,i}^{(0)} = 0.8$, with $i = 1, 2, ..., N$.

filtering radius and the total cell volume fraction being set as $R_n = R_0 \, l_{y\_n}/l_y$ $V_T^* = V_c^* + V_e^*$. In the calculations, R_0 and l_y are set as 150 μm and 4 mm, respectively, and l_{y_n} is the height of the scaling biobot. The varying R_n can ensure the topological similarity with the total cell number increase.

Fig. 5 shows that increasing cell number leads to a greater objective output for the optimized biobots. In this example, the abdominal parts degenerate from struts into robust ribs due to the increase in the filtering radius R_n (Aage et al., 2017), which indicates a jump of the objective function value (Fig. 5). While the topological features for cardiomyocytes are similar to the example shown in Fig. 4(b). It should be noted that the scaling process does not consider organism growth, and thus the cellular topologies of these organisms are independent of each other.

4.2. Effects of nutrient concentration

In this section, the first example in Fig. 4(a) is further used to profoundly study the effects of nutrient concentration ΔC on the multicellular topologies and objective functions.

Fig. 6(a) displays that nutrient concentration ΔC falls within a specific interval [0.2, 2.0], with each case terminating after 80 iterations. The amplitude values of the objective functions gradually increase with concentration ΔC while the final optimized topologies remain relatively stable. According to Eq. (7), an increase in nutrient concentration ΔC results in a larger active force $\mathbf{P}_{\text{bio}-\text{chemo}}$, thereby fostering enhanced actuation capabilities for the optimized biobot with a specific topological architecture.
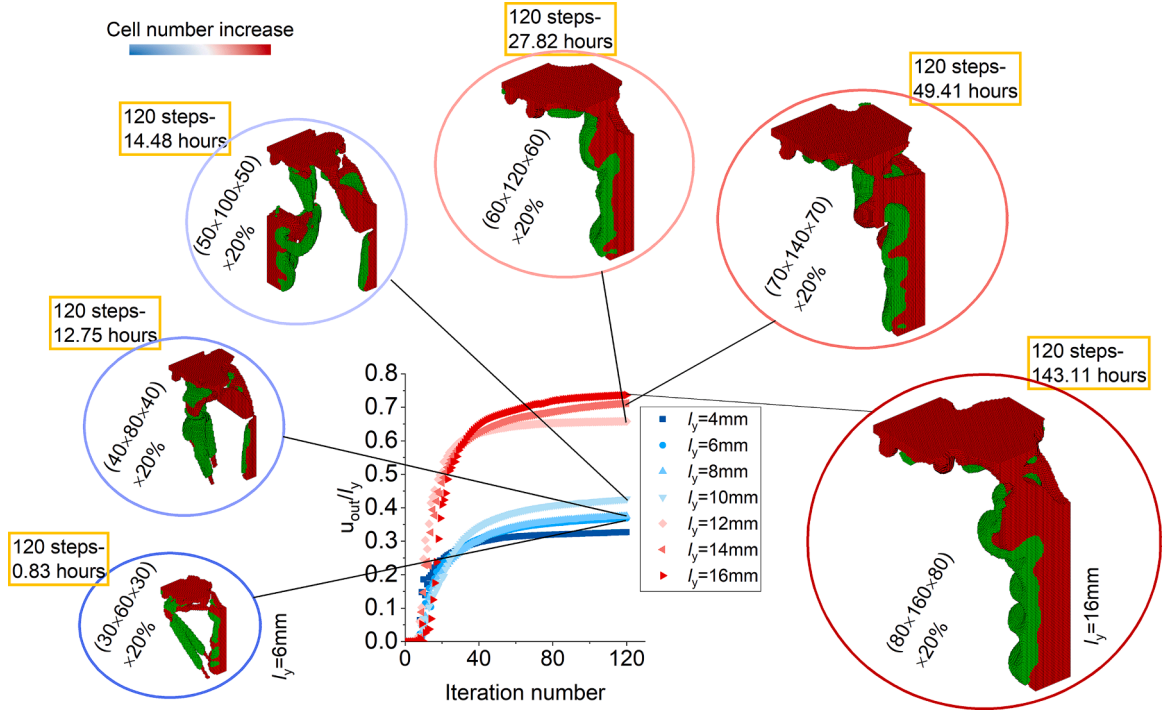
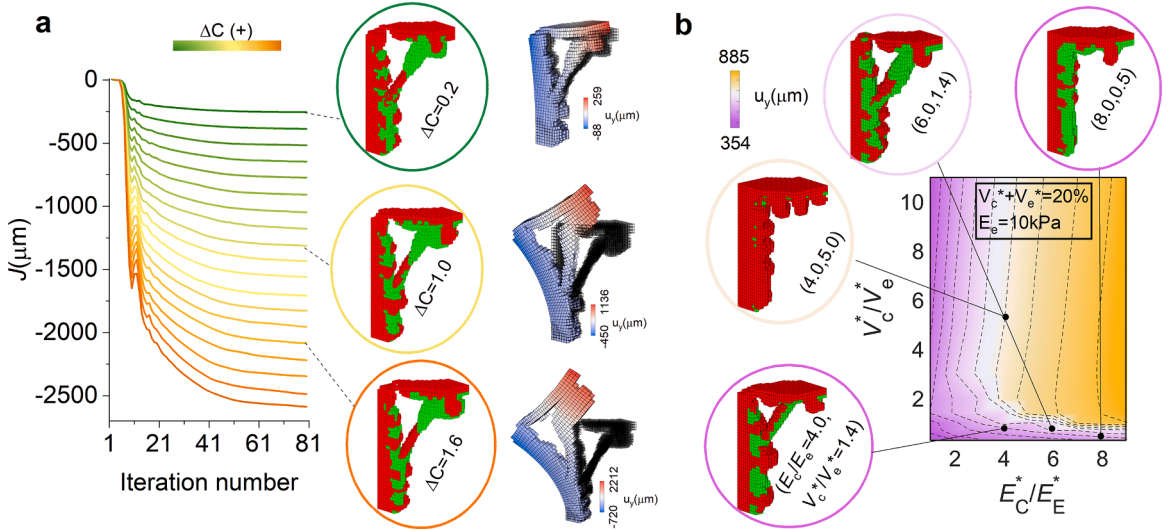**Fig. 5.** Effects of total cell numbers on the optimized multicellular biobots.

Fig. 6. Effects of the varying parameters, such as (a) nutrient concentration ΔC, and (b) E_c/E_e and V_c^*/V_e^* on the optimized multicellular biobots.

4.3. Cellular stiffness and volume fractions

In reality, accurately quantifying the modulus of individual cells in multicellular samples poses a challenge. Additionally, in a specified nutrient environment with constant concentration ΔC, the total active forces of an optimized biobot change with the fluctuations in the number of cardiomyocytes. All these uncertain factors play important roles in sculpting the functions and topologies of the biobots and need to be unveiled systematically.

Hence, it is imperative to investigate the impacts of $E_c/E_e \in \{1, 2, ..., 9\}$ and $V_c^*/V_e^* \in \{0.33, 0.5, 0.7, 1.0, 1.4, 2.0, 3.0, 5.0, 11.0\}$ on both the optimized topologies and functionalities, where the epidermal cell modulus and cell volume fraction satisfy $E_e = 10$ kPa and $V_c^* + V_e^* = 20\%$, respectively. In Fig. 6(b), the cases falling within the purple region exhibit lower output values compared to those in the yellow region. This is attributed to that the lower cell moduli of cardiomyocytes in the left purple region provide the biobot with a
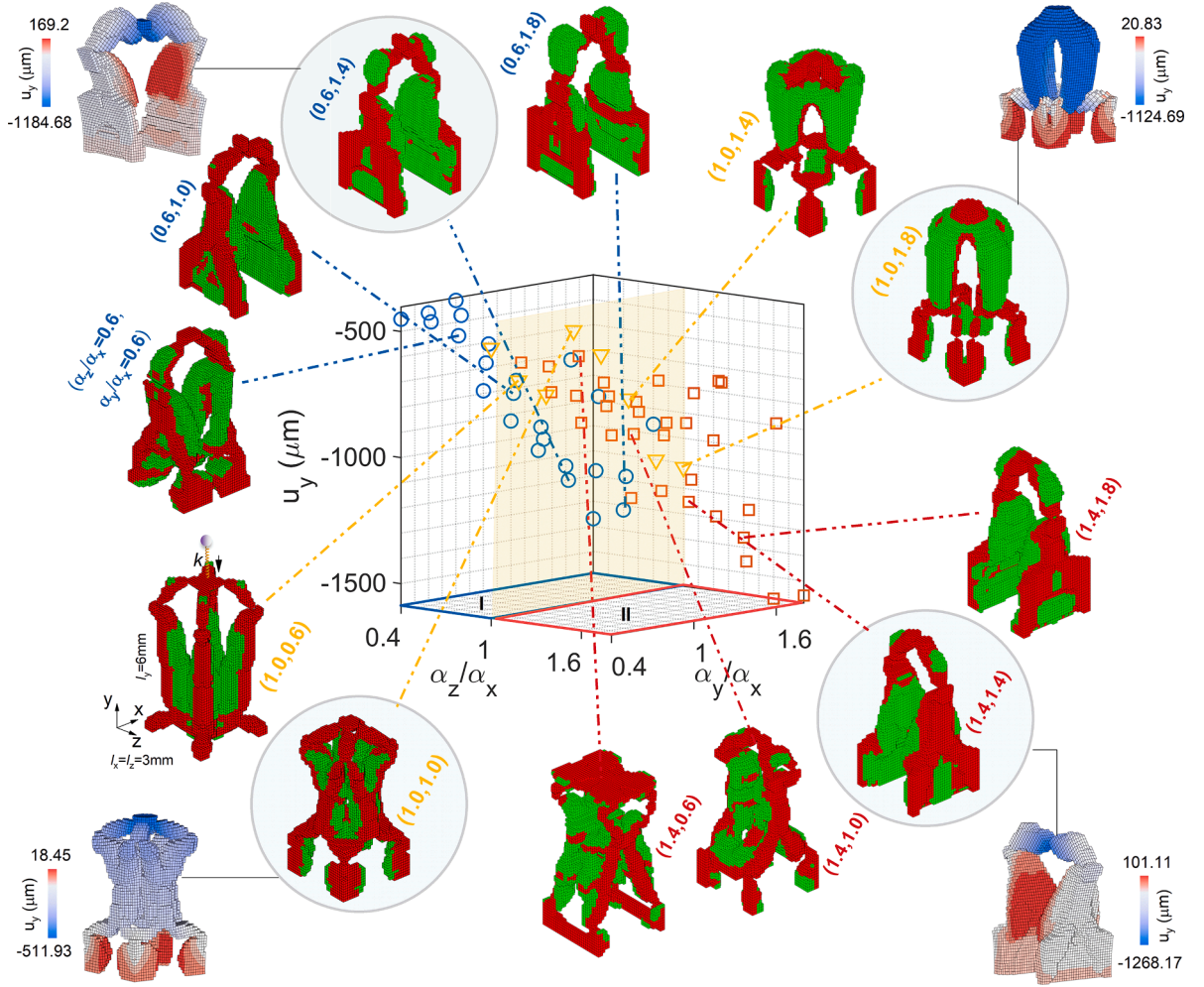
Fig. 7. Effects of anisotropic cardiomyocyte contractions on the optimized biobots.

lower stiffness to resist a larger active force than the cases in the yellow region. Additionally, the biobot tends to develop abdominal struts to enhance their stiffness when the modulus or number of cardiomyocytes decreases.

Based on our analysis, the instances located on the white region [Fig. 6(b)] represent an optimal combination of $(E_c /E_e, V_c^* /V_e^*)$, such as the case of (6.0, 1.4), offering a reasonable topology and excellent functionality. This finding provides a valuable insight into designing multicellular functional organoids based on the self-assembling or cell-printing methods.

4.4. Anisotropic contraction of cardiomyocytes

In this section, we unveil the effects of anisotropic biomechanical behaviors of cardiomyocytes (Avazmohammadi et al., 2019), such as contraction intensity, on the optimized results, by assuming that the coefficients α_x, α_y, and α_z have different values. The contraction coefficients and nutrient concentration satisfy $\alpha_x = -0.1$ and α_y/α_x, $\alpha_z/\alpha_x \in \mathbb{N} = \{0.2 : 0.2 : 1.8\}$, and $\Delta C = 0.4$, respectively. A total of 64 samples are considered, each having specific values of $V_c^* = 10\%$ and $V_e^* = 10\%$. The design domain size is $l_x \times l_y \times l_z = 3 \times 6 \times 3$ mm^3 (Fig. 7), corresponding to the element number of $30 \times 60 \times 30$.

In Fig. 7(a), the contraction strength along the x-direction is stronger than that along the z-direction in the region-I with $\alpha_z /\alpha_x < 1.0$, leading to the layout of cardiomyocytes being aligned along the x-direction in the optimized biobots. As the value of α_z /α_x increases gradually to 1.0, the active contraction becomes equal in both the x- and z-directions, resulting in symmetrical topological characteristics in the x-z plane. In region-II (Fig. 7), the layout of cardiomyocytes in the optimized biobots is oriented along the z-direction due to $\alpha_z/\alpha_x > 1.0$. This finding implies that the anisotropic contraction may promote the topology polarity of the biobots, which recruits cardiomyocytes to enhance their stiffness and functionalities.

Moreover, with the increasing contraction intensity of cardiomyocytes in the y-direction, their distribution becomes more concentrated in this direction (Fig. 7), which ultimately leads to an enhancement in the output of biobots.
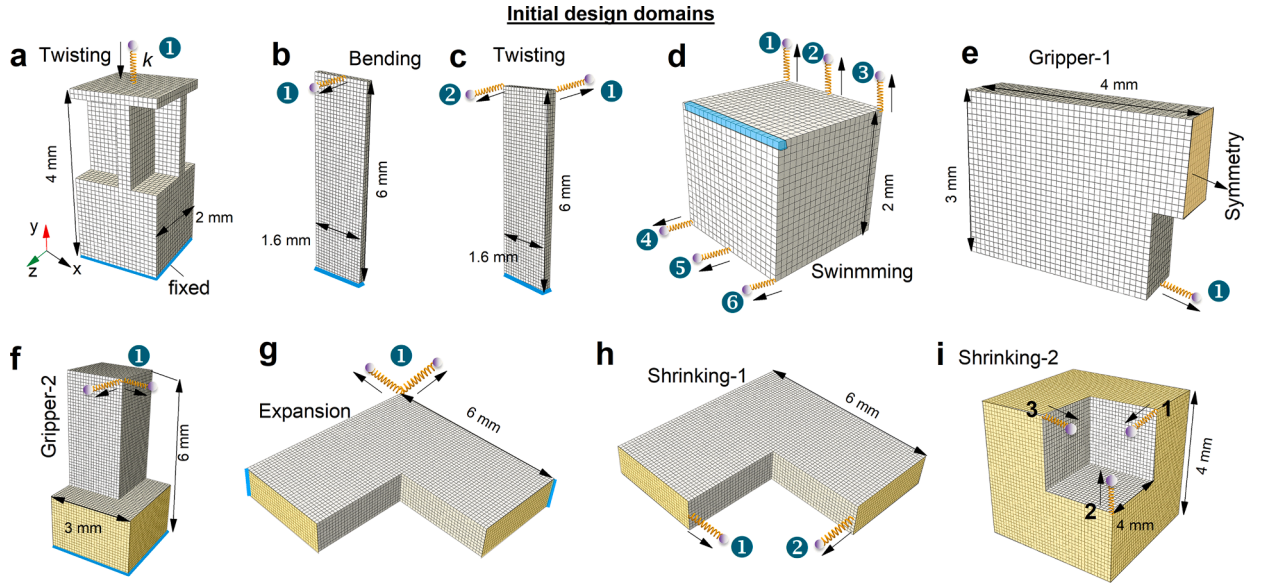
Initial design domains

Fig. 8. Optimization conditions, objective functions, boundary conditions, and design domains for various multifunction designs. (a) Twisting-cellular actuator. (b) Bending-cellular sheet. (c) Twisting-cellular sheet. (d) Swimming biobot, and the objective function is $\max : (\mathbf{L}_{1\_y}^{T} + \mathbf{L}_{2\_y}^{T} + \mathbf{L}_{3\_y}^{T})\mathbf{u} + (\mathbf{L}_{4\_z}^{T} + \mathbf{L}_{5\_z}^{T} + \mathbf{L}_{6\_z}^{T})\mathbf{u}$, where the first and second terms represent the summation of nodal displacements along the y and z-directions, respectively. (e, f) Cellular grippers. (g) An expanding-cellular biobot. (h, i) Shrinking-cellular biobots, and a quarter and an eighth domain with sizes of $l_x \times l_z \times l_y = 6 \times 6 \times 1$ mm^3 and $l_x \times l_z \times l_y = 6 \times 6 \times 6$ mm^3, respectively. The objective functions are defined as $\max : (\mathbf{L}_{1\_x}^{T} + \mathbf{L}_{2\_y}^{T})\mathbf{u}$ and $\max : (\mathbf{L}_{1\_x}^{T} + \mathbf{L}_{2\_y}^{T} + \mathbf{L}_{3\_z}^{T})\mathbf{u}$, respectively. The blue and yellow represent fixed and symmetrical boundary conditions, respectively. Here, we set the initial design variables $x_{1,i}^{(0)} = x_{2,i}^{(0)} = 0.8$, where $i = 1, 2, ..., N$.

4.5. Biobots with different functions

In this section, we further use the above method to predict four other types of biobots with different biomechanical functions (Filippia et al., 2022). The optimization details of these examples are given in Fig. 8, and Fig. A(1,2) in Appendix A.

(i) *Twisting biobots*

It is hard to design micro-sized twisting active biobots due to the specific requirements of chiral topological structures. Recently, advancements have been made in the design of intelligent twisting micro-architectures (Cui et al., 2022; Frenzel et al., 2017; Li et al., 2022) and medical robots (Ze et al., 2022). However, it remains unknown how one can design multicellular systems with self-propelled twisting function.

In Fig. 9(a), we propose an optimized biobot that has a clockwise or anti-clockwise twisting function due to the chiral topology of cardiomyocytes and epidermal cells by introducing chiral non-designable domains [Fig. 8(a)]. The objective function is defined as the maximum nodal displacement along the negative y-direction on the top surface and it is written as $\min : \mathbf{L}_{1\_y}^{T}\mathbf{u}$, where $\mathbf{L}_{1\_y}$ denotes the point index vector, as shown in Fig. 8(a).

Additionally, to enable the biobot to carry cargo on its top surface, a layer of element meshes to the top surface is composed of epidermal cells. All nodes of the elements on the bottom surface are fixed to prevent any movement. To avoid the inclination of the biobot, the nodal freedoms along the x- and z-directions of the vertical center line are also fixed. The volume fractions of cells are $V_c^* = V_e^* = 10\%$.

In Fig. 9(a), the chiral structures provide the whole organism with an active resultant twisting moment that ultimately drives the biobot to rotate. Moreover, the twisting angles θ of the top surfaces change from $5.61°$ to $16.62°$ with the nutrient concentrations ΔC ranging from 0.2 to 0.6.

(i) *Multicellular 'fish fins'*

The bell tissue of jellyfish (Costello et al., 2021; Lee et al., 2022; Park et al., 2016) [Fig. 9(b)] is composed of cardiomyocytes, epidermal and nerve cells, inspiring us to design a multicellular system with biomechanical functions similar to fish fins (Costello et al., 2021; Lee et al., 2022; Nawroth et al., 2012). To this end, two types of sheet-like structures [Fig. 8(b and c)] are taken as designable spaces. To achieve the bending function, the size of the design domain is $l_x \times l_y \times l_z = 1.6 \times 6 \times 0.2$ mm^3, and the designable space has two-layers of element meshes in the z-direction, as depicted in Fig. 8(b). The back layer is composed of only epidermal cells, while the
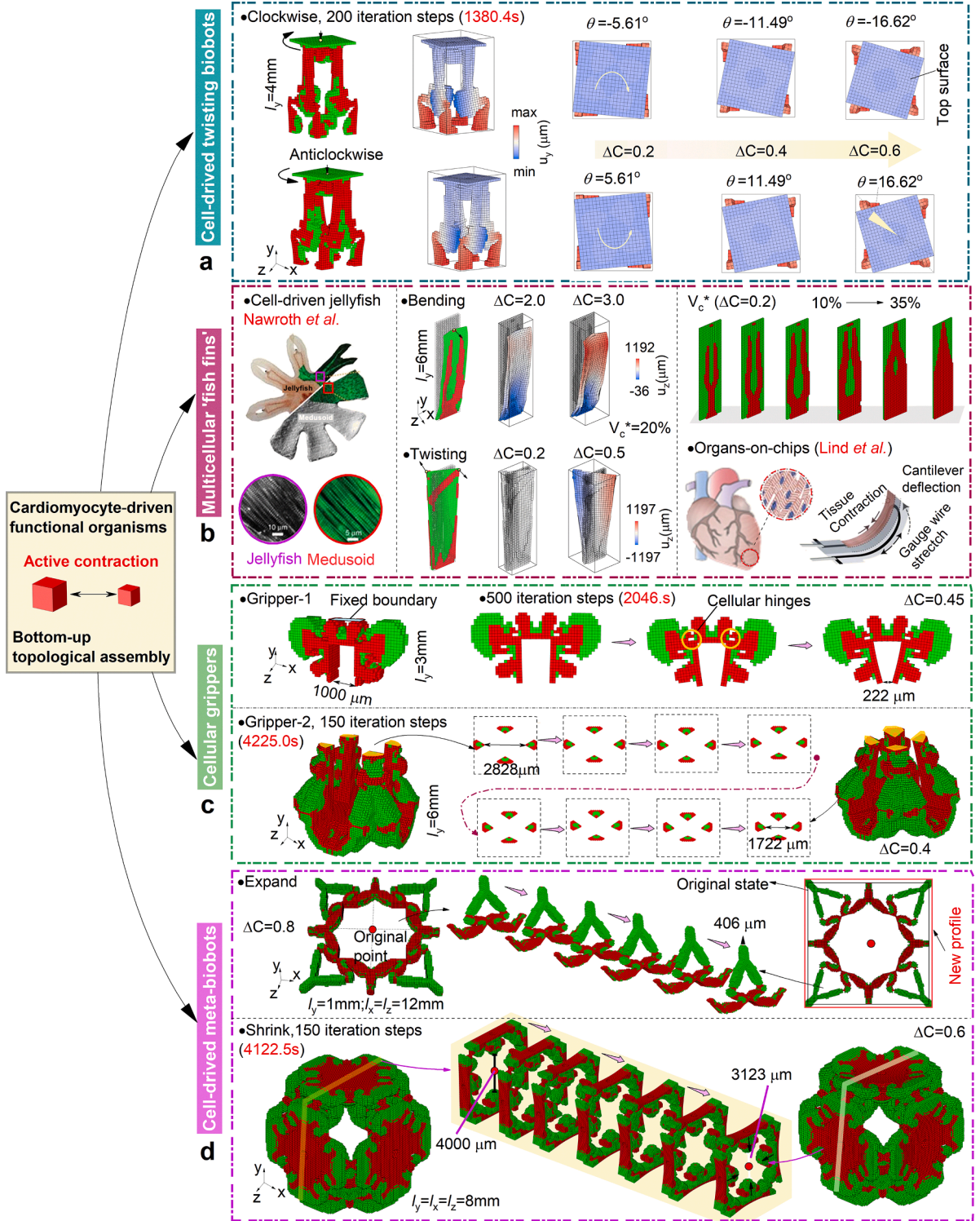
Fig. 9. Cardiomyocyte-driven functional biobots. (a) Twisting-cellular actuators. (b) Optimized cellular sheets obtain functions similar to Jellyfish and Medusoid fins. Adopted from Nawroth et al. (2012) with permission. These optimized cell-driven biobots can be used as organ-on-chip devices. Adopted from Lind et al. (2017) with permission. (c) Cellular grippers. (d) Expanding and shrinking meta-biobots.

front layer serves as a space that can be designed with cardiomyocytes. The volume fraction of the cardiomyocytes is $V_c = 20\,\%$. The objective function is chosen as $\max : \mathbf{L}_{1\_z}^T \mathbf{u}$, where $\mathbf{L}_{1\_z}$ is the nodal index vector, as shown in Fig. 8(b). In Fig. 9(b), cardiomyocytes are located in the central region of the cellular sheet, and their number gradually decreases from the bottom to the top regions. Owing to this topology of cardiomyocytes, the biobot can overcome the boundary constraint on the bottom surface. In Fig. 9(b), for example, the output displacement of the optimized biobot is 690.41 μmwith the nutrient concentration $\Delta C = 2.0$. Similarly, both the concentration and cardiomyocyte number also impact the biobot functionalities, as shown in Fig. 9(b). Further, the cell-driven sheets have a potential for drug screening in organ-on-chip biomedical engineering (Lind et al., 2017).

In terms of a three-layer cellular sheet [Fig. 9(c)], the design domain is given by $l_x \times l_y \times l_z = 0.3 \times 6 \times 1.6\,\text{mm}^3$, and the middle layer is filled with epidermal cells. The objective function is formulated as $\max : (\mathbf{L}_{2\_z}^T - \mathbf{L}_{1\_z}^T)\mathbf{u}$, where the nodal index vectors $\mathbf{L}_{1\_z}$ and $\mathbf{L}_{2\_z}$ are shown in Fig. 8(c). This objective function means that the displacement difference along the z-direction promotes the two nodes to move in opposite directions. Therefore, the distribution shapes of the cardiomyocytes on the back and front layers are completely opposite, which yields a periodic torsion for the optimized biobot [Fig. 9(b)]. Besides, biobots that have similar topologies to the *Xenobot* (Kriegmana et al., 2020) are shown in Figs. 8(d), and A1(a,b) (Appendix A).

(i) *Cellular grippers*

Skeletal muscle tissue has been proposed to provide the power that drives a microscopic gripper (Morimoto et al., 2018). Such hybrid robots allow a pick-and-place manipulation of objects through an integration of two functional parts. Using the above-proposed method, we here design multicellular microscopic grippers with the functionality of grasping objects (Leveziel et al., 2022; Xu et al., 2024).

In Fig. 8(e), the size of the half design domain for gripper-1 is $l_x \times l_y \times l_z = 4 \times 3 \times 1\,\text{mm}^3$. The volume fractions and nutrient concentration within this domain are specified as $V_c^* = V_e^* = 10\,\%$ and $\Delta C = 0.45$, respectively. We take the objective function $\max : \mathbf{L}_{1\_x}^T \mathbf{u}$. In Fig. 9(c), the cellular gripper is composed of cardiomyocytes supported by epidermal cells located on the outer space. Due to the cellular hinges (Yellow circle), the distance of the two chucks dynamically changes from 1000 μm to 222 μm, driven by cardiomyocytes (Fig. A1, Appendix A).

A similar strategy is taken to design a biobot containing four chucks. In Fig. 8(f), the size of the quarter design space is $l_x = l_y = l_z = 3 \times 6 \times 3\,\text{mm}^3$. The volume fractions and nutrient concentration within this region are $V_c^* = V_e^* = 10\,\%$ and $\Delta C = 0.40$, respectively. The objective function is specified as $\max : (\mathbf{L}_{1\_x}^T + \mathbf{L}_{1\_z}^T)\mathbf{u}$. In Fig. 9(c), the distance of the four chucks changes from 2828 μm to 1722 μmduring the contraction process [Fig. A1(e), Video S2 in Supplementary materials and Appendix A]. These two examples demonstrate a great potential to obtain multicellular systems with grasping functionality through optimal design of their topologies.

(i) *Cell-driven meta-biobots*

In metamaterials, specific microstructural topologies are often designed to endow the macroscopic material with exotic physical behaviors, such as negative thermal expansion. Although the thermal expansion coefficient of the basal material is positive, the microstructure ultimately shrinks its volume due to the specific topology structures of the unit cell (Sigmund and Torquato, 1997; Wang et al., 2016). By analogy, cardiomyocytes can be regarded as a living material with negative thermal expansion coefficients. In what follows, we consider whether it is possible or not to obtain an expanding multicellular organism driven by cardiomyocytes through topology design.

A quarter designable domain is shown in Fig. 8(g), with a size of $l_x \times l_z \times l_y = 6 \times 6 \times 1\,\text{mm}^3$. The volume fraction and nutrient concentration are $V_c^* = V_e^* = 10\,\%$ and $\Delta C = 0.8$, respectively, and the objective function is defined as $\min : (\mathbf{L}_{1\_x}^T + \mathbf{L}_{1\_z}^T)\mathbf{u}$. The optimized biobot depicted in Fig. 9(d) possesses a remarkable ability to expand its body driven by cardiomyocytes [Fig. A1(f)], which is beneficial to specific topological hinges that push the corners to move away from the original center (red point). For comparison, we illustrate an example of cell-driven shrinking biobot as shown in the bottom part of Figs. 9(d), and A1(g,h) (Appendix A and Video S3 in Supplementary materials), where the central regions of the six surfaces get close to the original point.

Taken together, we have designed four types of biobots that exhibit distinct biomechanical functions. Although only two types of cells have been used, we achieve distinct functions by utilizing different bottom-up topology assembling modes. However, it is worth noticing that a key issue in the assembly of cellular aggregates is the realization of the complex 3D topology of multicellular biobots. Fortunately, significant progress has been made in this direction, owing to the rapidly developing sacrificial ink (Bertassoni, 2022; Zhang et al., 2021), cryopreservation (Luo et al., 2022), and multi-axis bioprinting (Zhang et al., 2022b) technologies. In the extrusion-based sacrificial printing approach, for example, the bioink containing living cells swiftly solidifies into an organ structure upon contact with a supportive microgel bath. The supportive bath helps the multicellular topological organs to resist collapse. After the removal of the sacrificial gel support, the printed topological organs may exhibit favorable biological and mechanical performance (Zhang et al., 2021). In this technique, the impacts of cell-to-cell adhesion and cell–bioink interaction on the optimized multicellular organs remain unclear and deserve further endeavors.

4.6. Applications of collective biobots

Biology systems can be seen as a collaboration among numerous individuals, resulting in complex and interconnected dynamical
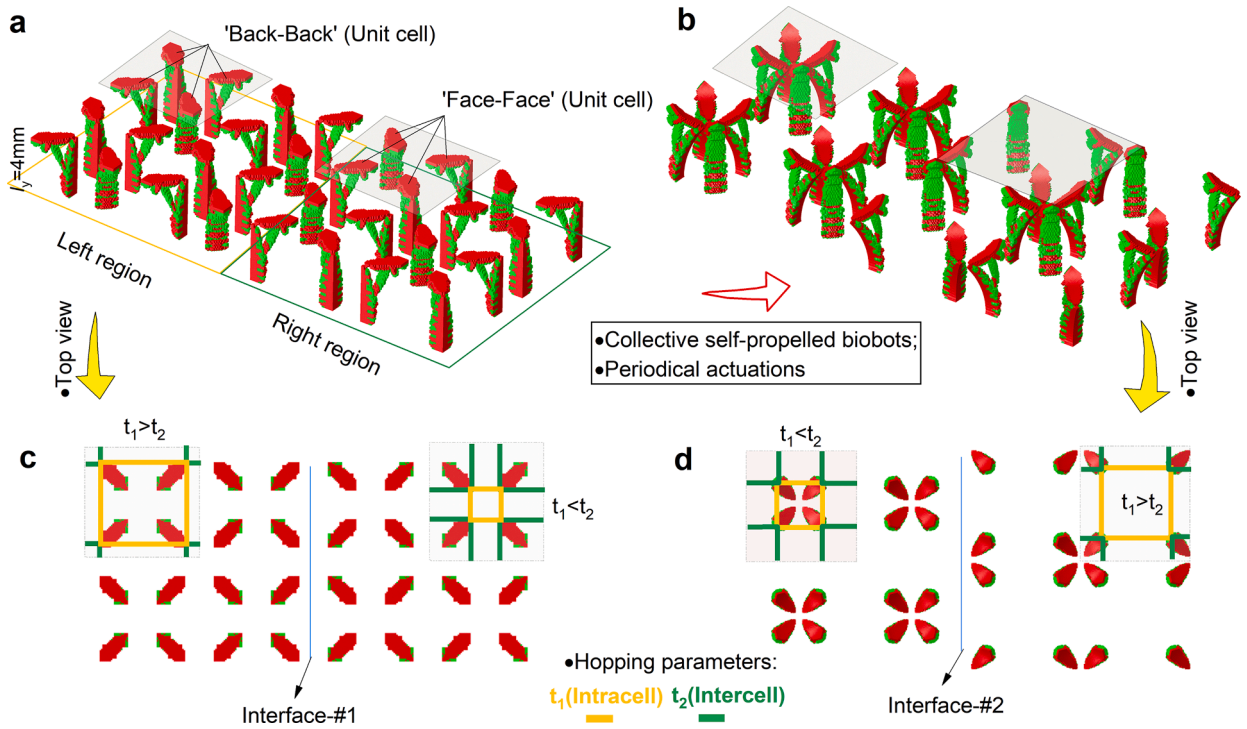
Fig. 10. Living topological materials driven by collective biobots. (a, b) Original state of the collective biobots, and the coupling strengths $t_1(\Delta C) > t_2(\Delta C)$ in the left region and $t_1(\Delta C) < t_2(\Delta C)$ in the right region. (c, d) Self-propelled states of the living collective biobots with the coupling strengths being $t_1(\Delta C) < t_2(\Delta C)$ in the left region and $t_1(\Delta C) > t_2(\Delta C)$ in the right region.

behaviors (Li et al., 2019; Lin et al., 2021). In the tumor microenvironment, for example, such immune cells as T lymphocytes and dendritic cells (Schwartzberg et al., 2009; Shi et al., 2018) interact with cancer cells (Oyler-Yaniv et al., 2017), thereby influencing tumor growth and the effectiveness of immunological therapies (Gungabeesoon et al., 2023; Zhou et al., 2023). In this subsection, therefore, we will present two types of collective biobots with specific physical and medical functions. It is anticipated that the biobots could work in a collective environment to achieve specific functions.

(i) *Living topological materials*

Fig. 10(a) presents a type of collective organisms, comprising 32 biobots obtained from the proposed optimization method [Fig. 4 (b)]. In Fig. 10(a) and (b), the biobots located at the left and right regions have different unit cells composed of biobots with 'back-back' and 'face-face' modes, respectively. We use the hopping parameters t_1 and t_2 to denote the biobot head distances in the unit cell [Fig. 10(c)]. They are affected by the active mechanical actuations driven by the nutrient concentration ΔC. At the initial moment, the hopping parameters satisfy $t_1(\Delta C) > t_2(\Delta C)$ (left region) and $t_1(\Delta C) < t_2(\Delta C)$(right region), while they become $t_1(\Delta C) < t_2(\Delta C)$ (left region) and $t_1(\Delta C) > t_2(\Delta C)$ (right region) when the collective biobots start to actuate, as shown in Fig. 10(c and d). Consequently, the interface mode between the left and right regions also changes from interface #1 to #2. Based on the classical Su–Schrieffer–Heeger (SSH) model (Haldane, 1988; Yao and Wang, 2018; Zhang et al., 2023), the changes in the hopping parameters on both sides of the living interface affect the energy distributions and topological invariants of the collective biobots. Additionally, the collective self-propelled spinning biobots are also shown in Fig. B1 (Appendix B). These assembled biobots hold potential for the design of living topological materials (Dorrah and Capasso, 2022; Semeghini et al., 2021; Zhang et al., 2023).

(i) *High-throughput drug screening*

Rapid and effective screening of drugs is important for the treatment of various diseases (Yellen et al., 2021), including the world-spreading coronavirus disease (COVID-19) (Mirabelli et al., 2021). Traditional methods of drug testing and screening not only prolong the process but also result in lower efficacy during the final clinical stages (Ma et al., 2020). The rapidly developing *in vitro* organoids emerges as a new technology for drug screening. Organoids can not only replicate some biological functions of target organs but also provide reliable physiological and pathological environments (Ao et al., 2022).

Recent advancements in high-throughput drug screening using *in vitro* organoids have occurred in various treatments, such as SARS-CoV-2 viral infection (Mirabelli et al., 2021), Alzheimer's disease (HiPSC-driven cerebral organoid) (Park et al., 2021), and human cardiac problem (HiPSC-driven in vitro cardiac organoids) (Goldfracht et al., 2019; Lee et al., 2023; Mills et al., 2019). In the
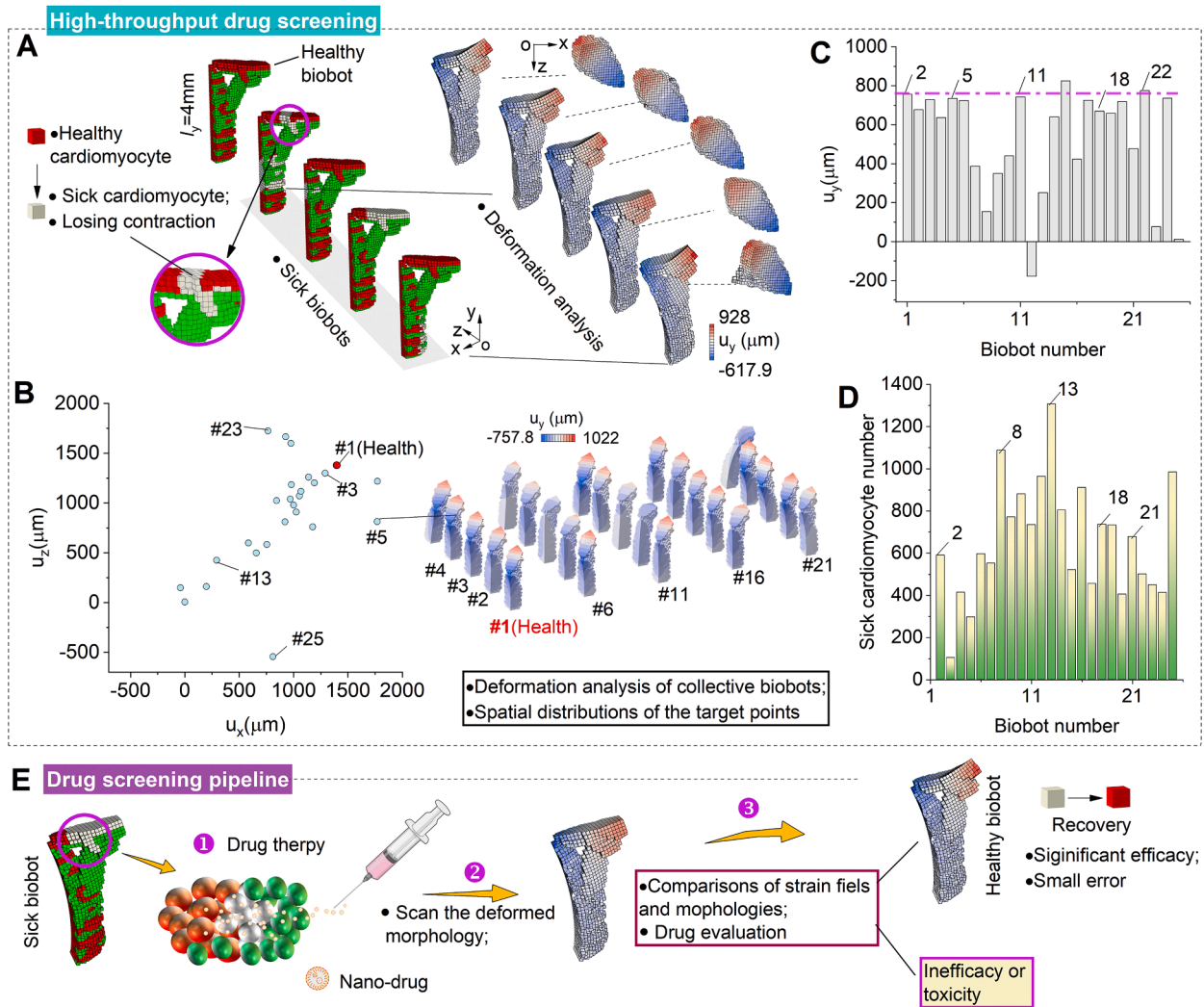
Fig. 11. High-throughput drug screening pipeline using the collective multicellular biobots. (a) Different biomechanical behaviors between the healthy and sick biobots. (b) Displacements of the target points are projected in the *x-z* plane. (c) Displacements of the target points. (d) Diseased cardiomyocyte numbers. (e) An effective high-throughput drug screening pipeline.

cardiac organoids, drug effectiveness is determined by measuring their changes in body sizes and contraction frequencies. In our optimized biobots with specific functionalities, the measurement process could be more convenient. For example, it is easy to track the displacements of the optimized output points. In the context of collective biobots, there would exist noticeable disparities in the functional output behaviors between healthy and diseased biobots, indicating novel prospects for drug screening.

In Fig. 11(a), we depict the healthy and diseased states of various biobots, assuming that in the diseased states, a few cardiomyocytes lose their active contraction ability (white cells). Numerical simulations indicate significant disparities in biomechanical behaviors between the diseased and healthy biobots, as shown in Fig. 11(a). The discrepancies arise because the inactive contraction capability of sick cardiomyocytes disrupts the normal deformation morphologies of the entire organism, consequently resulting in spatial distribution changes in their deformation as illustrated in Fig. 11(b–d) and B2 (Appendix B and Video S4 in Supplementary materials). The severity of organism illness correlates with the degree to which the optimized target points deviate from their healthy positions in the *x-z* plane [red dot in Fig. 11(f)], which is beneficial to performing drug screening.

Fig. 11(e) outlines the drug screening process by using a biobot with three steps. First, the targeted nanoparticle drug is delivered to the diseased regions. In the second step, after a specific treatment period, the spatial deformations of the recovered biobots are scanned and compared with those of the healthy biobots. In the context of biobot population treatment, a substantial volume of data concerning the deformations of recovered biobots can be acquired for the next step. Finally, if their resemblances to healthy biobot deformations are significant, the designed drug is considered effective. Conversely, a significant or inconspicuous deviation between the two sets of deformations might indicate potential toxicity or ineffectiveness.

5. Conclusions

Based on the topology optimization method, we have proposed an inverse theory to design 3D multicellular biobots composed of cardiomyocytes and passive epidermal cells, aiming to achieve targeted biomechanical functions in both individual and collective biobots. Through extensive simulations, we have examined the impacts of such factors as cellular numbers, elastic moduli, and anisotropic contractions on the topologies and functions of biobots. The proposed method demonstrates the potential of functional biobots capable of exhibiting exotic actuations, such as self-propelled torsion, expansion and grasping objects, and presenting diverse living topological interfaces within collective biobots. We have also discussed the potential applications of such collective biobots for high-throughput drug screenings.

However, the proposed multicellular topological assembly method still faces some limitations and challenges. For example, we have not considered the polarity uncertainty of cardiomyocytes during self-assembly or cell printing (Runser et al., 2023; Stevens et al., 2023; Zhang et al., 2022b). Incorporating this mechanism into the optimization models is crucial for designing efficient organisms (Ren and Han, 2019; Takebe and Wells, 2019). In addition, it is also of interest to incorporate the growth, topological evolution and physiological environments of multicellular functional systems (Buske et al., 2011; Clawson and Levin, 2023; Norfleet et al., 2020), such as hearts (Drakhlis et al., 2021; Yonatan R. Lewis-Israeli et al., 2021) or tumor-immunity organoids (LeSavage et al., 2022; Ren and Han, 2019; Tuveson and Clevers, 2019). Finally, it is emphasized that the machine learning method (Jumper et al., 2021; Sanchez-Lengeling and Aspuru-Guzik, 2018; Zohdi, 2022) and the other cell models (Van Liedekerke et al., 2020; Sun et al., 2022) can be implemented into the proposed inverse theory for designing multicellular functional systems. These issues all merit further efforts.

CRediT authorship contribution statement

Hui-Kai Zhang: Writing – review & editing, Writing – original draft, Visualization, Validation, Supervision, Software, Resources, Project administration, Methodology, Investigation, Formal analysis, Data curation, Conceptualization. **Bo-Wen Xu:** Writing – original draft, Data curation. **Zi-Yao Jia:** Writing – original draft, Data curation. **Bo Li:** Writing – original draft, Data curation. **Xi-Qiao Feng:** Writing – review & editing, Writing – original draft, Visualization, Validation, Supervision, Resources, Project administration, Investigation, Funding acquisition, Formal analysis, Data curation.

Declaration of competing interest

The authors declare that they have no known competing financial interests or personal relationships that could have appeared to influence the work reported in this paper.

Data availability

Data will be made available on request.

Supplementary materials

Supplementary material associated with this article can be found, in the online version, at doi:10.1016/j.jmps.2024.105634.
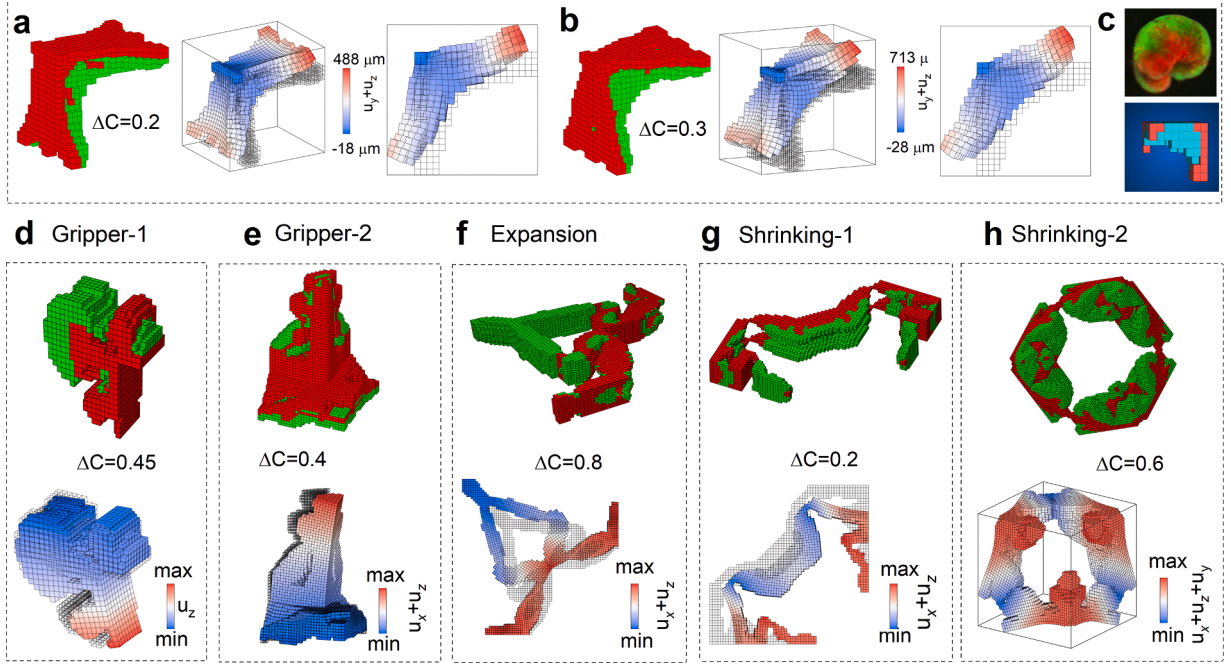
Appendix A

Fig. A1. Deformation analysis of the optimized results. (a, b) The cellular topologies of the optimized biobots are similar to the *Xenobot* [Fig. 1(e)] in (c). (d, e) Cellular grippers. (f) Expanding deformation. (g, h) Shrinking deformation related to Fig. 8(h) and (i).
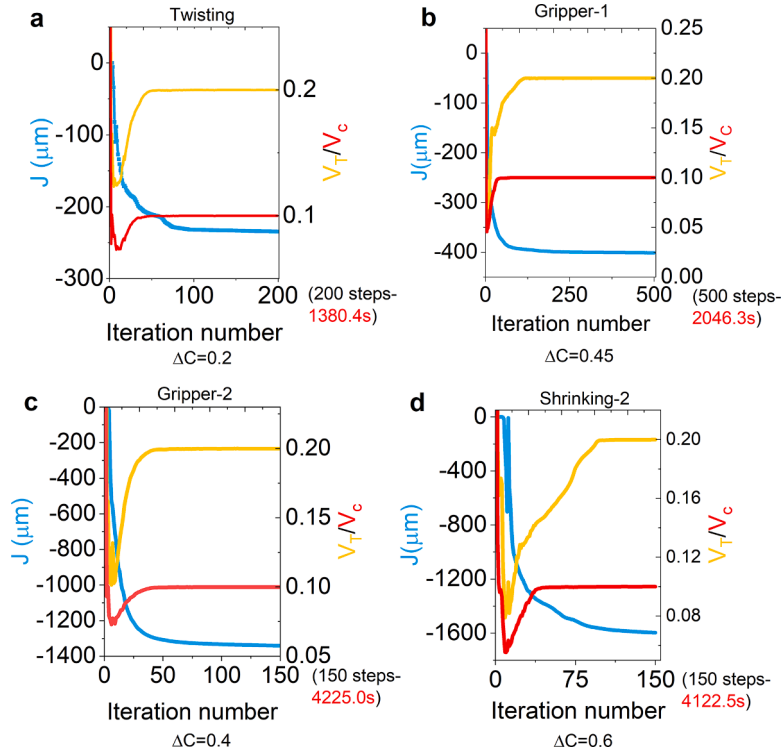

Fig. A2. Iteration histories. (a) Twisting biobot. (b, c) Cellular gripper-1 and gripper-2. (d) Shrinking organism.
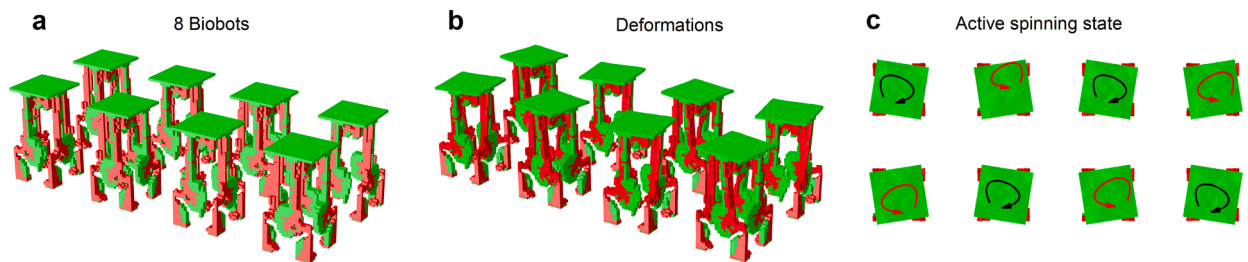
Appendix B

Fig. B1. Spinning behaviors of collective biobots. (a) Collective biobots (Fig. 9A). (b, c) Self-propelled spinning states.
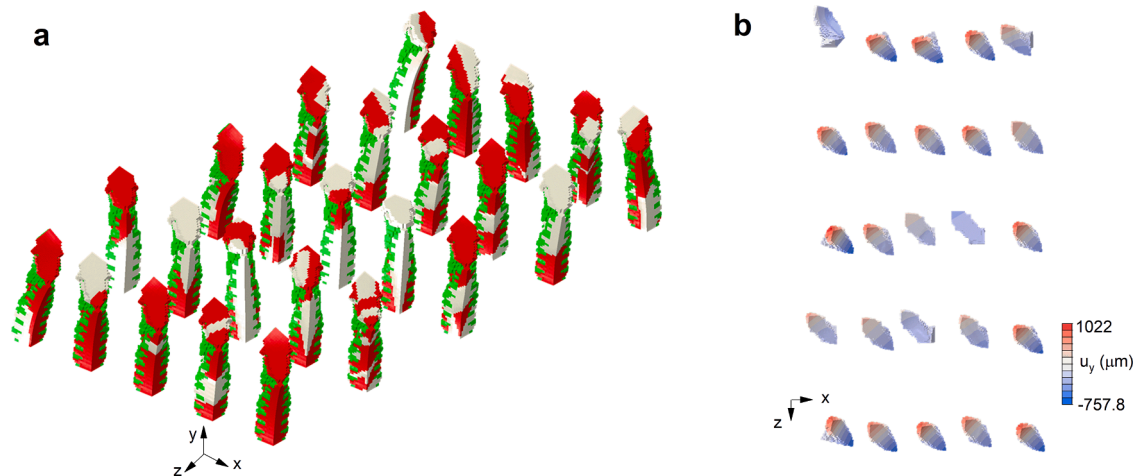

Fig. B2. Deformations of collective biobots [Fig. 11(b)]. (a) Healthy cardiomyocytes (red), healthy epidermal cells (green) and sick cardiomyocytes (white). (b) Deformations in the view of the *x-z* plane.

References

https://www.biomap.com/zh/research-projects/ 2023.

https://www.bostondynamics.com/ 2023.

Aage, N., Andreassen, E., Lazarov, B.S., Sigmund, O., 2017. Giga-voxel computational morphogenesis for structural design. Nature 550, 84–86.

Alford, P.W., Feinberg, A.W., Sheehy, S.P., Parker, K.K., 2010. Biohybrid thin films for measuring contractility in engineered cardiovascular muscle. Biomaterials 31, 3613–3621.

Ao, Z., Cai, H.W., Wu, Z.H., Hua, L.Y., Nuneza, A., Zhou, Z.L., et al., 2022. Microfluidics guided by deep learning for cancer immunotherapy screening. Proc. Natl. Acad. Sci. U. S. A. 119, 2214569119.

Avazmohammadi, R., Soares, J.S., Li, D.S., Raut, S.S., Gorman, R.C., Sacks, M.S., 2019. A contemporarylook at biomechanical models of myocardium. Annu. Rev. Biomed. Eng. 21, 417–442.

Bath, J., Green, S.J., Allen, K.E., Turberfield, A.J., 2009. Mechanism for a directional, processive, and reversible DNA motor. Small 5, 1513–1516.

Bendsoe, M.P., Sigmund, O., 1999. Material interpolation schemes in topology optimization. Arch. Appl. Mech. 69, 635–654.

Bertassoni, L.E., 2022. Bioprinting of complex multicellular organs with advanced functionality—recent progress and challenges ahead. Adv. Mater. 34, 2101321.

Bol, M., Reese, S., Parker, K.K., Kuhl, E., 2009. Computational modeling of muscular thin films for cardiac repair. Comput. Mech. 43, 535–544.

Buske, P., Galle, J., Barker, N., Aust, G., Clevers, H., Loeffler, M., 2011. A comprehensive model of the spatio-temporal stem cell and tissue organisation in the intestinal crypt. PLoS Comput. Biol. 7, e1001045.

Chen, L.W., Jia, Y.Q., Wang, F.W., Sigmund, O., Zhang, X.J.S., 2023. Programming and physical realization of extreme three-dimensional responses of metastructures under large deformations. Int. J. Eng. Sci. 191, 103881.

Cheng, X., Fan, Z.C., Yao, S.L., Jin, T.Q., Lv, Z.Y., Lan, Y., et al., 2023. Programming 3D curved mesosurfaces using microlattice designs. Science 379, 1225–1232.

Clawson, W.P., Levin, M., 2023. Endless forms most beautiful 2.0: teleonomy and the bioengineering of chimaeric and synthetic organisms. Biol. J. Linn. Soc. 139, 457–486.

Costello, J.H., Colin, S.P., Dabiri, J.O., Gemmell, B.J., Lucas, K.N., Sutherland, K.R., 2021. The hydrodynamics of jellyfish swimming. Annu. Rev. Mar. Sci. 13, 375–396.

Cui, H.C., Yao, D.S., Hensleigh, R., Lu, H.T., Calderon, A., Xu, Z.P., et al., 2022. Design and printing of proprioceptive three-dimensional architected robotic metamaterials. Science 376, 1287–1293.

Dorrah, A.H., Capasso, F., 2022. Tunable structured light with flat optics. Science 376, eabi6860.

Drakhlis, L., Biswanath, S., Farr, C.M., Lupanow, V., Teske, J., Ritzenhoff, K., et al., 2021. Human heart-forming organoids recapitulate early heart and foregut development. Nat. Biotechnol. 39, 737–746.

Elston, T., Wang, H.Y., Oster, G., 1998. Energy transduction in ATP synthase. Nature 391, 510–513.

Feinberg, A.W., Feigel, A., Shevkoplyas, S.S., Sheehy, S., Whitesides, G.M., Parker, K.K., 2007. Muscular thin films for building actuators and powering devices. Science 317, 1366–1370.

Filippia, M., Yasaa, O., Kammb, R.D., Ramanc, R., Katzschmanna, R.K., 2022. Will microfluidics enable functionally integrated biohybrid robots. Proc. Natl. Acad. Sci. U. S. A. 119, 2200741119.

Frenzel, T., Kadic, M., Wegener, M., 2017. Three-dimensional mechanical metamaterials with a twist. Science 358, 1072–1074.

Gao, L., Akhtar, M.U., Yang, F., Ahmad, S., He, J.K., Lian, Q., et al., 2021. Recent progress in engineering functional biohybrid robots actuated by living cells. Acta Biomaterialia 121, 29–40.

Gao, T., Zhang, W.H., 2010. Topology optimization involving thermo-elastic stress loads. Struct. Multidiscip. Optim. 42, 725–738.

Geiss, M.J., Boddeti, N., Weeger, O., Maute, K., Dunn, M.L., 2019. Combined level-set-xFEM-density topology optimization of four-dimensional printed structures undergoing large deformation. J. Mech. Des. 141, 051405.

Goktepe, S., Abilez, O.J., Kuhl, E., 2010. A generic approach towards finite growth with examples of athlete's heart, cardiac dilation, and cardiac wall thickening. J. Mech. Phys. Solids 58, 1661–1680.

Goldfracht, I., Efraim, Y., Shinnawi, R., Kovalev, E., Huber, I., Gepstein, A., et al., 2019. Engineered heart tissue models from hiPSC-derived cardiomyocytes and cardiac ECM for disease modeling and drug testing applications. Acta Biomater. 92, 145–159.

Goriely, A., 2018. Five ways to model active processes in elastic solids: active forces, active stresses, active strains, active fibers, and active metrics. Mech. Res. Commun. 93, 75–79.

Guix, M., Mestre, R., Patino, T., De Corato, M., Fuentes, J., Zarpellon, G., et al., 2021. Biohybrid soft robots with self-stimulating skeletons. Sci. Robot. 6, abe7577.

Gumuskaya, G., Srivastava, P., Cooper, B.G., Lesser, H., Semegran, B., Garnier, S., et al., 2023. Motile living biobots self-construct from adult human somatic progenitor seed cells. Adv. Sci., 2303575

Gungabeesoon, J., Gort-Freitas, N.A., Kiss, M.t., Bolli, E., Messemaker, M., Siwicki, M., et al., 2023. A neutrophil response linked to tumor control in immunotherapy. Cell 186, 1448–1464.

Haldane, F.D.M., 1988. Model for a quantum hall-effect without landau-levels - condensed-matter realization of the parity anomaly. Phys. Rev. Lett. 61, 2015–2018.

Hamel, C.M., Roach, D.J., Long, K.N., Demoly, F., Dunn, M.L., Qi, H.J., 2019. Machine-learning based design of active composite structures for 4D printing. Smart Mater. Struct. 28, 065005.

Ibusuki, R., Morishita, T., Furuta, A., Nakayama, S., Yoshio, M., Kojima, H., et al., 2022. Programmable molecular transport achieved by engineering protein motors to move on DNA nanotubes. Science 375, 1159–1164.

Jia, H.Y., Flommersfeld, J., Heymann, M., Vogel, S.K., Franquelim, H.G., Bruckner, D.B., et al., 2022. 3D printed protein-based robotic structures actuated by molecular motor assemblies. Nat. Mater. 21, 703–709.

Jiang, J.H., Ranabhat, K., Wang, X.Y., Rich, H., Zhang, R., Peng, C.H., 2022. Active transformations of topological structures in light-driven nematic disclination networks. Proc. Natl. Acad. Sci. U. S. A. 119, e2122226119.

Jumper, J., Evans, R., Pritzel, A., Green, T., Figurnov, M., Ronneberger, O., et al., 2021. Highly accurate protein structure prediction with AlphaFold. Nature 596, 583–589.

Kaczmarski, B., Moulton, D.E., Goriely, A., Kuhl, E., 2023. Bayesian design optimization of biomimetic soft actuators. Comput. Methods Appl. Mech. Eng. 408, 115939.

Keller, P., 2002. Shape the vertebrate body plan by polarized embryonic cell movements. Science 298, 1950–1954.

Kriegman, S., Blackistona, D., Levina, M., Bongardc, J., 2021. Kinematic self-replication in reconfigurable organisms. Proc. Natl. Acad. Sci. U. S. A. 118, e2112672118.

Kriegmana, S., Blackiston, D., Levin, M., Bongard, J., 2020. A scalable pipeline for designing reconfigurable organisms. Proc. Natl. Acad. Sci. U. S. A. 117, 1853–1859.

Kumar, P., Langelaar, M., 2021. On topology optimization of design-dependent pressure-loaded three-dimensional structures and compliant mechanisms. Int. J. Numer. Methods Eng. 122, 4787, 4787.

Lee, K.Y., Park, S.J., Matthews, D.G., Kim, S.L., Marquez, C.A., Zimmerman, J.F., et al., 2022. An autonomously swimming biohybrid fish designed with human cardiac biophysics. Science 375, 639–647.

Lee, S.W., Song, M.J., Woo, D.H., Jeong, G.S., 2023. Assessment of the optimal generation period and size of human iPSC-derived cardiac organoids for cardiotoxicity drug testing. Preprint.

LeSavage, B.L., Suhar, R.A., Broguiere, N., Lutolf, M.P., Heilshorn, S.C., 2022. Next-generation cancer organoids. Nat. Mater. 21, 143–159.

Leveziel, M., Haouas, W., Laurent, G.J., Gauthier, M., Dahmouche, R., 2022. MiGriBot: a miniature parallel robot with integrated gripping for high-throughput micromanipulation. Sci. Robot. 7, eabn4292.

Li, S.C., Lerch, M.M., Waters, J.T., Deng, B.L., Martens, R.S., Yao, Y.X., et al., 2022. Self-regulated non-reciprocal motions in single-material microstructures. Nature 605, 76–83.

Li, S.G., Batra, R., Brown, D., Chang, H.D., Ranganathan, N., Hoberman, C., et al., 2019. Particle robotics based on statistical mechanics of loosely coupled components. Nature 567, 361–365.

Lin, S.Z., Zhang, W.Y., Bi, D.P., Li, B., Feng, X.Q., 2021. Energetics of mesoscale cell turbulence in two-dimensional monolayers. Commun. Phys. 4, 1–8.

Lind, J.U., Busbee, T.A., Valentine, A.D., Pasqualini, F.S., Yuan, H.Y., Yadid, M., et al., 2017. Instrumented cardiac microphysiological devices via multimaterial three-dimensional printing. Nat. Mater. 16, 303–308.

Luo, Z.Y., Tang, G.S., Ravanbakhsh, H., Li, W.L., Wang, M.A., Kuang, X., et al., 2022. Vertical extrusion cryo(bio)printing for anisotropic tissue manufacturing. Adv. Mater. 34, 2108931.

Ma, C., Peng, Y.S., Li, H.D., CHen, W.Q., 2020. Organ-on-a-chip: a new paradigm for drug development. Trends Pharmacol. Sci. 42, 119–133.

Mathur, A.B., Collinsworth, A.M., Reichert, W.M., Kraus, W.E., Truskey, G.A., 2001. Endothelial, cardiac muscle and skeletal muscle exhibit different viscous and elastic properties as determined by atomic force microscopy. J. Biomech. 34, 1545–1553.

Mills, R.J., Parker, B.L., Quaife-Ryan, G.A., Voges, H.K., Needham, E.J., Bornot, A., et al., 2019. Drug screening in human PSC-cardiac organoids identifies pro-proliferative compounds acting via the mevalonate pathway. Cell Stem Cell 24 (6), 895–907 e6.

Mirabelli, C., Wotring, J.W., Zhang, C.J., McCarty, S.M., Fursmidt, R., Prettoc, C.D., et al., 2021. Morphological cell profiling of SARS-CoV-2 infection identifies drug repurposing candidates for COVID-19. Proc. Natl. Acad. Sci. U. S. A. 118, e2105815118.

Mizuno, D., Tardin, C., Schmidt, C.F., MacKintosh, F.C., 2007. Nonequilibrium mechanics of active cytoskeletal networks. Science 315, 370–373.

Morimoto, Y., Onoe, H., Takeuchi, S., 2018. Biohybrid robot powered by an antagonistic pair of skeletal muscle tissues skeletal muscle tissues. Sci. Robot. 3, eaat4440.

Nawroth, J.C., Lee, H., Feinberg, A.W., Ripplinger, C.M., McCain, M.L., Grosberg, A., et al., 2012. A tissue-engineered jellyfish with biomimetic propulsion. Nat. Biotechnol. 30, 792–797.

Nitta, T., Wang, Y.Z., Du, Z., Morishima, K., Hiratsuka, Y., 2021. A printable active network actuator built from an engineered biomolecular motor. Nat. Mater. 20, 1149–1155.

Noj, H., Yasudat, R., Yoshida, M., Kinosita, K., 1997. Direct observation of the rotation of F1-ATPase. Nature 386, 299–302.

Norfleet, D.A., Park, E., Kemp, M.L., 2020. Computational modeling of organoid development. Curr. Opin. Biomed. Eng. 13, 113–118.

Oyler-Yaniv, A., Oyler-Yaniv, J., Whitlock, B.M., Liu, Z.D., Germain, R.N., Huse, M., et al., 2017. A tunable diffusion-consumption mechanism of cytokine propagation enables plasticity in cell-to-cell communication in the immune system. Immunity 46, 609–620.

Paetsch, C., Trimmer, B.A., Dorfmann, A., 2012. A constitutive model for active-passive transition of muscle fibers. Int. J. Non Linear Mech. 47, 377–387.

Park, J.C., Jang, S.Y., Lee, D.J., Lee, J.H., Kang, U., Chang, H.J., et al., 2021. A logical network-based drug-screening platform for Alzheimer's disease representing pathological features of human brain organoids. Nat. Commun. 12, 1–13.

Park, S.J., Gazzola, M., Park, K.S., Park, S., Di Santo, V., Blevins, E.L., et al., 2016. Phototactic guidance of a tissue-engineered soft-robotic ray. Science 353, 158–162.

Ravanbakhsh, H., Zhang, Y.S., 2022. Cryobioprinting for biomedical applications. J. 3D Print. Med. 6, 163–166.

Regazzoni, F., Dede, L., Quarteroni, A., 2021. Active force generation in cardiac muscle cells: mathematical modeling and numerical simulation of the actin-myosin interaction. Vietnam J. Math. 49, 87–118.

Ren, C.L., Han, C.X., 2019. Organoids-preclinical models of human disease. N. Engl. J. Med. 380, 1981, 1981.

Runser, S., Vetter, R., Iber, D., 2023. 3D simulation of tissue mechanics with cell polarization bioRxiv preprint.

Sanchez-Lengeling, B., Aspuru-Guzik, A., 2018. Inverse molecular design using machine learning: generative models for matter engineering Science, 361, 360–365.

Sato, Y., Kobayashi, H., Yuhn, C.Y., Kawamoto, A., Nomura, T., Kikuchi, N., 2021. Topology optimization of locomoting soft bodies using material point method. Struct. Multidiscip. Optim. 66, 1–7.

Schwartzberg, P.L., Mueller, K.L., Qi, H., Cannons, J.L., 2009. SLAM receptors and SAP influence lymphocyte interactions, development and function. Nat. Rev. Immunol. 9, 39–46.

Semeghini, G., Levine, H., Keesling, A., Ebadi, S., Wang, T.T., Bluvstein, D., et al., 2021. Probing topological spin liquids on a programmable quantum simulator. Science 374, 1242–1247.

Shi, J.W., Hou, S.Y., Fang, Q., Liu, X., Liu, X.L., Qi, H., 2018. PD-1 controls follicular T helper cell positioning and function. Immunity 49, 264–274.

Sigmund, O., 2001a. Design of multiphysics actuators using topology optimization - Part I: one-material structures. Comput. Methods Appl. Mech. Eng. 190, 6577–6604.

Sigmund, O., 2001b. Design of multiphysics actuators using topology optimization - Part II: two-material structures. Comput. Methods Appl. Mech. Eng. 190, 6605–6627.

Sigmund, O., Torquato, S., 1997. Design of materials with extreme thermal expansion using a three-phase topology optimization method. J. Mech. Phys. Solids 45, 1037–1067.

Stevens, A.J., Harris, A.R., Gerdts, J., Kim, K.H., Trentesaux, C., Ramirez, J.T., et al., 2023. Programming multicellular assembly with synthetic cell adhesion molecules. Nature 614, 144–152.

Sun, S.Y., Zhang, H.X., Fang, W., Chen, X.D., Li, B., Feng, X.Q., 2022. Bio-chemo-mechanical coupling models of soft biological materials: a review. Adv. Appl. Mech. 55, 309–392.

Svanberg, K., 1987. The method of moving asymptotes - a new method for structural optimization. Int. J. Numer. Methods Eng. 24, 359–373.

Takebe, T., Wells, J.M., 2019. Organoids by design. Science 364, 956–959.

Tian, J.W., Li, M.Q., Han, Z.H., Chen, Y., Gu, X.F.D., Ge, Q.J., et al., 2022. Conformal topology optimization of multi-material ferromagnetic soft active structures using an extended level set method. Comput. Methods Appl. Mech. Eng. 389, 114394.

Toda, S., Blauch, L.R., Tang, S.K.Y., Morsut, L., Lim, W.A., 2018. Programming self-organizing multicellular structures with synthetic cell-cell signaling. Science 361, 156–162.

Tuveson, D., Clevers, H., 2019. Cancer modeling meets human organoid technology. Science 364, 952–955.

Van Liedekerke, P., Neitsch, J., Johann, T., Warmt, E., Gonzàlez-Valverde, I., Hoehme, S., Grosser, S., Kaes, J., Drasdo, D., 2020. A quantitative high-resolution computational mechanics cell model for growing and regenerating tissues. Biomech. Model. Mechanobiol. 19, 189–220.

Wang, Q.M., Jackson, J.A., Ge, Q., Hopkins, J.B., Spadaccini, C.M., Fang, N.X., 2016. Lightweight mechanical metamaterials with tunable negative thermal expansion. Phys. Rev. Lett. 117, 175901.

Wang, Y.Z., Nitta, T., Hiratsuka, Y., Morishima, K., 2022. In situ integrated microrobots driven by artificial muscles built from biomolecular motors. Sci. Robot. 7, aba8212.

Xu, H.F., Wu, S., Liu, Y., Wang, X.P., Efremov, A.K., Wang, L., McCaskill, J.S., Medina-Sánchez, M., Schmidt, O.G., 2024. 3D nanofabricated soft microrobots with super-compliant picoforce springs as onboard sensors and actuators. Nat. Nanotechnol. 1–10.

Xue, S.N., Su, Y.J., Xu, C.G., Xu, M.G., Yao, R., 2023. Heterogeneous liver tissues with multicellular crosstalk and bile duct morphogenesis through organoid bioprinting. Preprint available at Research Square 10.21203/rs.3.rs-2727920/v1.

Yao, S.Y., Wang, Z., 2018. Edge states and topological invariants of non-Hermitian systems. Phys. Rev. Lett. 121, 086803.

Yellen, B.B., Zawistowski, J.S., Czech, E.A., Sanford, C.I., SoRelle, E.D., Luftig, M.A., et al., 2021. Massively parallel quantification of phenotypic heterogeneity in single-cell drug responses. Sci. Adv. 7, eabf9840.

Lewis-Israeli, Y.R., Wasserman, A.H., Gabalski, M.A., Volmert, B.D., Ming, Y., Ball Xanthippi Chatzistavrou, K.A., et al., 2021. Self-assembling human heart organoids for the modeling of cardiac development and congenital heart disease. Nat. Commun. 12, 5142.

Yuhn, C.Y., Sato, Y., Kobayashi, H., Kawamoto, A., Nomura, T., 2023. 4D topology optimization: integrated optimization of the structure and movement of self-actuating soft bodies. Comput. Methods Appl. Mech. Eng. 414, 116187.

Ze, Q.J., Wu, S., Nishikawa, J., Dai, J.Z., Sun, Y., Leanza, S., et al., 2022. Soft robotic origami crawler. Sci. Adv. 8, eabm7834.

Zhang, H.K., Chen, W.T., Xu, S.H., Wu, J., Li, B., Feng, X.Q., 2023. Active topological phase transitions in high-order elastic topological insulators driven by pneumatic methods and liquid metals. J. Appl. Phys. 133, 104504.

Zhang, H.K., Zhou, J.Y., Fang, W., Zhao, H.C., Zhao, Z.L., Chen, X.D., et al., 2022a. Multi-functional topology optimization of Victoria cruziana veins. J. R. Soc. Interface 19, 20220298.

Zhang, Y.S., Haghiashtiani, G., Hübscher, T., Kelly, D.J., Lee, J.M., Luto, M., et al., 2021. 3D extrusion bioprinting. Nat. Rev. Methods Prim. 1 (1), 75.

Zhang, Z.Y., Wu, C.M., Dai, C.K., Shi, Q.q., Fang, G.X., Xie, D.F., et al., 2022b. A multi-axis robot-based bioprinting system supporting natural cell function preservation and cardiac tissue fabrication. Bioact. Mater. 18, 138–150.

Zhao, Z., Zhang, X.J.S., 2022. Topology optimization of hard-magnetic soft materials. J. Mech. Phys. Solids 158, 104628.

Zhou, Z.Z., Pang, Y., Ji, J.Y., He, J.Y., Liu, T.K., Ouyang, L.L., et al., 2023. Harnessing 3D in vitro systems to model immune responses to solid tumours: a step towards improving and creating personalized immunotherapies. Nat. Rev. Immunol. 1–15.

Zohdi, T.I., 2022. Machine-learning and digital-twins for rapid evaluation and design of injected vaccine immune-system responses. Comput. Methods Appl. Mech. Eng. 2022, 115315.